AD_____

Award Number: DAMD17-99-1-9379

TITLE: Improving Detection of Axillary Lymph Nodes by Computer-Aided Kinetic Feature Identification in Positron Emission Tomography

PRINCIPAL INVESTIGATOR: Xiaoli Yu, Ph.D.

CONTRACTING ORGANIZATION: University of Southern California
Los Angeles, California 90023

REPORT DATE: August 2000

TYPE OF REPORT: Annual

PREPARED FOR: U.S. Army Medical Research and Materiel Command
Fort Detrick, Maryland 21702-5012

DISTRIBUTION STATEMENT: Approved for Public Release;
Distribution Unlimited

The views, opinions and/or findings contained in this report are those of the author(s) and should not be construed as an official Department of the Army position, policy or decision unless so designated by other documentation.

REPORT DOCUMENTATION PAGE

Form Approved
OMB No. 074-0188

1. AGENCY USE ONLY (Leave blank)	2. REPORT DATE	3. REPORT TYPE AND DATES COVERED
	August 2000	Annual (1 Aug 99 - 31 Jul 00)

4. TITLE AND SUBTITLE
Improving Detection of Axillary Lymph Nodes by Computer-Aided Kinetic Feature Identification in Positron Emission Tomography

5. FUNDING NUMBERS
DAMD17-99-1-9379

6. AUTHOR(S)
Xiaoli Yu, Ph.D.

7. PERFORMING ORGANIZATION NAME(S) AND ADDRESS(ES)
University of Southern California
Los Angeles, California 90023

E-MAIL:
xiyu@milly.usc.edu

8. PERFORMING ORGANIZATION REPORT NUMBER

9. SPONSORING / MONITORING AGENCY NAME(S) AND ADDRESS(ES)
U.S. Army Medical Research and Materiel Command
Fort Detrick, Maryland 21702-5012

10. SPONSORING / MONITORING AGENCY REPORT NUMBER

11. SUPPLEMENTARY NOTES
This report contains colored photos

12a. DISTRIBUTION / AVAILABILITY STATEMENT
Approved for public release; distribution unlimited

12b. DISTRIBUTION CODE

13. ABSTRACT ***(Maximum 200 Words)***
This project seeks to improve detection of metastatic axillary breast cancer and decrease a number of unnecessary breast biopsies through developing a sophisticated statistical signal processing system to aid identification of metabolic information within dynamic PET data. This Year 1 effort has been concentrated on mathematical modeling, validity analysis and algorithm development. We have found some interesting, natural relationship of conventional PET-FDG kinetic modeling to subspace representation in linear algebra. By representing time-activity curves of normal and malignant tissues with distinct subspaces, the distance between the subspaces can quantitatively characterize the difference between normal and malignant tissues as well as the similarity between primary and metastatic lesions. It turns out that OSEM outperforms FBP in revealing such difference and similarity. To accelerate the subspace estimation performed on a fully reconstructed dynamic image sequence, the validity of estimating parameters directly from projection data prior to the image reconstruction has been studied. With such estimations, a data compression algorithm has been developed for a fast dynamic image reconstruction, which maximizes the signal-to-noise ratio (SNR). Our results have shown in both theory and simulation that this new algorithm is superior to the conventional principal components method in enhancing SNR of small lesions.

14. SUBJECT TERMS
Breast Cancer, axillary disease, PET, statistical signal processing

15. NUMBER OF PAGES
71

16. PRICE CODE

17. SECURITY CLASSIFICATION OF REPORT	18. SECURITY CLASSIFICATION OF THIS PAGE	19. SECURITY CLASSIFICATION OF ABSTRACT	20. LIMITATION OF ABSTRACT
Unclassified	Unclassified	Unclassified	Unlimited

NSN 7540-01-280-5500

Standard Form 298 (Rev. 2-89)
Prescribed by ANSI Std. Z39-18
298-102

Table of Contents

1 Introduction

PET provides a 80% high sensitivity for detection of the primary breast malignancy, as well as for axillary metastatic disease. What remains at issue is an inaccuracy rate high as 20% is not acceptable to replace the invasive breast biopsies. For this reason, further improvements in detectability of malignancy in the axilla through use of in vivo statistical imaging processing techniques are warranted. This project seeks to improve detection of metastatic axillary breast cancer and decrease the number of unnecessary breast biopsies by exploiting and identifying the metabolic information contained within dynamic PET imaging data through developing and testing a sophisticated computer-aided diagnosis system. Our goal is to design an intelligent system to supplement, rather than replace, conventional diagnosis by visual inspection. The proposed study consists of four proven tasks: **Task 1:** Developing the mathematical formula to linearly map and identify the physiological features contained in PET dynamic sinogram sequence (Month 1-8), **Task 2**: Developing the schemes for objective reduction of dynamic sinogram data guided by the identified TAC subspaces of the desired signal (tumor) and the interference (normal tissue background plus noise) (Month 4 - 12), **Task 3**: Deriving and analyzing statistical hypothesis test criteria to test the presence of an axillary metastasis in the dynamic images reconstructed from the compressed sinogram data (Month 13 - 24), and **Task 4**: Clinical Evaluation (Month 13 - 36). For each task, several subtasks were defined, see the SOW for details.

2 Body

During this annual reporting period, the effort is mainly concentrated on Tasks 1 and 2, the physiological feature modeling and identification and the objective rank-reduction of dynamic PET sinogram for fast image reconstruction, that were proposed for the first year. But studying on the rest tasks has also been performed. The major accomplishments of this activity are presented as follows. The technical details and related results can be found in Appendices.

2.1 PET-FDG tracer kinetic models and subspace representations (for Task 1).

This project was initiated by investigation of tracer kinetics. Study of tracer kinetics involves a radiolabeled biologically active compound (tracer) and a mathematical model that describes the tracer kinetics. Because FDG was proposed in our protocols for collecting clinical PET data, we have focused our attention on the PET-FDG kinetics study.

Through a literature search we have reviewed various types of mathematical models of PET-FDG kinetics and selected a three-compartmental model (also being called 4-K compartmental model) as a start. In a 4-k compartmental model for a homogeneous tissue, we found that each time activity curve (TAC) is composed of several basis TAC functions.

Feng and Wang [1] used a compartmentalized model to represent tracer behavior in the blood circulatory system, where the FDG plasma TAC was represented by a 4th-order exponential curve with a pure decay and a pair of repeated eigenvalues. In this case, the basis TAC functions are a set of exponential functions. But, if no special compartmental model is assumed on the arterial input function, then each basis TAC function is a exponential function in time convolved with the arterial input function [7]. These basis TAC functions span a subspace in terms of linear algebra, which implies that a subspace representation of a TAC is naturally achievable for modeled or arbitrary blood function.

The mathematical formula of TAC and its corresponding subspace representation for 4-K compartmental model has been extended to an arbitrary number of compartments. If certain conditions are fulfilled, e.g., initial conditions are zero, the solutions to the TAC will simply be the sum of basis TAC functions. Usually, the number of basis TAC functions is equal to the number of compartments in the model.

Due to the limited spatial resolution of the PET scanner and the forward and backward processes in a PET system, measurement of radioactivity in a homogeneous tissue is rarely, if ever achieved. For such reason, we also studied the mixture analysis or physiological factor analysis to incorporate the heterogeneity effects for a heterogeneous region of interest, where the mixed tissue TAC can be represented as the mass-weighted average of physiological function in each of the finite homogeneous tissues [2, 3]. For a mixed (heterogeneous) tissue pixel containing a finite number of J overlapping independent homogeneous compartments, each of which is described by a physiological factor, the TAC will be represented as a weighted sum of the J independent physiological functions. The physiological factors (using vector notation) define a subspace with dimension J embedded in a N-dimensional space. From the physiological factor analysis (PFA), the tissue TAC in PET is modeled as a linear combination of the fundamental physiological functions which are called *basis* in signal processing.

The details of this work on the compartmental modeling and subspace representation can be found in Appendix A, which is a chapter of the Ph. D. thesis (draft) by Mr. C. C. Huang.

2.2 Physiological subspace identification with PET projection data (for Task 1)

Estimation of subspace parameters was previously performed on tomographic images following reconstruction of the full dynamic sequence of projection data. The least square (LS) method of subspace identification based on image pixels was developed in [10] and is staightforwardly extended to a project-data-based approach during this report period. The software implementation of this extended LS algorithm is under development. Up to date the validity of applying other techniques proposed in [5, 6, 7] to perform subspace parameter estimation on projection data has also been investigated. The methods in [5, 6] are restricted to specific compartmental models. [7] used a more general modeling of spectral analysis, but only resulted in the impulse response function (IRF) estimation. Resolving the subspace paramters from the estimated IRF is to be studied.

2.3 A method of refining the physiological subspaces for enhancement of separability between lesions and normal tissues (for Task 1)

Our study on PET-FDG tracer kinetic models has been shown that the kinetic features of time activity curves (TAC) have the following properties: (a) linearly representable by a set of exponential functions, (b) physiologically distinguishable as lesion and normal tissue subspaces, (c) readily incorporable to a matched subspace detector for lesion detection.

To identify the TAC subspace features, we use the least square error (LSE) method to determine the lesion and normal tissue subspaces respectively. The subspaces resulted from the LSE are optimum in terms of the fidelity to the observed data, but they may suffer from a lack of the separability between subspaces. Therefore, we have made an effort to develop a new method to form the subspace representation of lesion and normal tissue kinetics, which maximizes the distance (separability) between lesion and normal tissue subspaces under the constraint that the LSE (fidelity) of the estimated and observed TACs is less than a given value. Such refined subspaces

are incorporated into our developed subspace identifier for performance test in terms of lesion detectability. Our results demonstrate that the subspaces identified by the new method from known lesion and normal tissues mostly preserve the TAC kinetic features and significantly increase the contrast of the small lesion to normal tissues compared to the LSE-only method.

This work has been presented in IEEE Medical Image Processing Conference 1999, Seattle, Wa. November 1999. The details are described in Appendix B.

2.4 A scheme of data compression for fast dynamic PET image reconstruction (for Task 2)

The reconstruction of dynamic PET images is time consuming. The objective of Task 2 is to accelerate this procedure. Previous work to speed up the dynamic image reconstruction was based on low-order approximation using Karhunen-Loève (KL) transform [8], [9]. Those KL transform basis vectors corresponding to the largest K eigenvalues were retained and then used in the reconstruction process. However, with this approach the kinetic characteristic (time activity curves) of week signals, such as non-palpable tumors, may be lost or significantly changed in the reconstructed images. In this effort, metrics are found to select a subset of vectors from the KL transform basis, which relates directly to maximizing signal-to-noise ratio (MSNR) or maximizing signal energy (MSE) only .

In this study, three rank-reduction criteria were applied to lower the dimensionality of dynamic sinogram in time domain. The simulation results show that by compressing the sinogram data before image reconstruction, one can speed up the reconstruction of dynamic images and also suppress the noise. The proposed maximum SNR criterion outperforms the conventional SVD and the maximum signal energy methods in terms of enhancing lesion to background contrast in the reconstructed images. From the measured time activity curves in the images reconstructed from the sinograms processed with the three different rank reduction criteria, one can see that the maximum SNR method maintains the characteristics of the lesion time activity curve, while both the SVD and the maximum signal energy methods change the characteristics of time activity curve in the lesion substantially. The results using computer simulation PET data show that by this approach the contrast of small lesion to the background can be objectively enhanced. The characteristic of time activity curve in the lesions can also be approximately kept.

Details of this new method can be found in Appendix C, which is a manuscript revised to be submit to IEEE Trans. on Medical Image Processing.

2.5 Comparison and evaluation of kinetic features contained in OSEM and FBP dynamic PET images (for Tasks 3 and 4)

Investigating the advantage of OSEM over FBP in revealing kinetic features contained in dynamic PET data is a part of the effort of Tasks 4.3 and 4.4. In this achievement, three types of kinetic features were used for the comparison: time activity curve (TAC), the compartmental modeling parameters and the physiological factors [4]. It is assumed that the physiological factors of metastases are similar to primary tumors. In this study the time activity curves (TAC) in the known lesions and normal tissues were measured from the clinical dynamic PET-FDG images reconstructed by OSEM and FBP algorithms, respectively. The mean square errors between the TACs obtained from the images reconstructed by the two algorithms were calculated. From the measured time activity curves k1-k4 PET-FDG compartmental parameters were estimated using the Newton-Raphson nonlinear parameter estimation. The estimated parameters from each set of

reconstructed images were clustered into parameter subregions according to tumor types (lung and breast) and tissue types (normal tissue, primary tumor, and metastasis). The distance between the clusters were computed and compared for the two reconstruction algorithms as a figure of merit for tumor detectability. Finally the physiological factors are identified using the both reconstructions by a statistical test criterion previously developed by our research group. Receiver operating characteristic (ROC) study on both reconstruction algorithms is performed with computer simulated phantom dynamic images. Clinical data from 16 patients (8 lung and 8 breast cancers) were used for the study. Our results show that no significant difference is observed in the TACs obtained from the OSEM and the FBP images, but the physiological factors identified from the metastases in OSEM images are substantially closer to those of the primary tumors than in FBP images. We found that the sensitivity of metastasis detection in the static FBP PET images can be improved using the physiological feature identification from the OSEM reconstructed dynamic images.

This work has been presented in SNM annual conference 2000, San Louise, Mo. June 2000, see Appendix D for details.

2.6 Patient data collection for clinical evaluation (Task 4)

An effort had been made to recruit a group of patients with biopsy proven primary breast cancer and palpable lymph node involvement at the USC County Hospital through Dr. Linda Hovanessian of the USC Radiology Department. Dr. Hovanessian recommended more than 20 patients for us to contact. Unfortunately, only a few of them were willing to take a PET scan. Discussions with Dr. Hovanessian concluded that patient's lack of knowledge about the project could be the key reason for this unwillingness. To remedy the problem, flyers with brief introduction of the project have been made by USC PET Center to deliver to the qualified patients. We have also contacted the group of Dr. Waiseman at USC Norris Breast Cancer Center and setup protocols with the group for patient recruit there. We believe all this can improve the patient recruiting.

3 Key Research Accomplishments

The main accomplishments in Year 1 are

- Studying various PET-FDG kinetic models in homogeneous and heterogeneous tissues and investigating the validity of subspace representations for time activity curves (TAC) in different tissues
- Establishing the subspace distance (or angle) as a measure to quantitatively characterize the difference between normal and malignant tissues as well as the similarity between primary and metastatic lesions
- Investigating methods to perform subspace parameter estimation directly on PET project data and extending the image-pixel-based least square subspace identification method to a scan-projection-based approach
- Developing a data compression algorithm, which is able to fast dynamic image reconstruction and simultaneously enhance lesion-to-background (or signal-to-noise) ratio; Comparing the new algorithm to the conventional principal components method (or SVD - singular value decomposition) in theory and simulation

- Comparing OSEM and FBP reconstructed images in terms of revealing the difference between normal and malignant tissues and the similarity between primary and metastatic lesions by performing a receiver operating characteristic (ROC) study on simulated phantom and clinical data
- Recruiting the desired patient data for clinical evaluation in coming years

4 List of Reportable Outcomes

1. C. C. Huang and X. Yu, "A New Method of Computer-Aided Feature Identification for Lesion Detection in PET-FDG Dynamic Study" *IEEE Medical Imaging Conference 1999, Seattle, WA, November 1999*
2. X. Yu, C. C. Huang and P. S. Conti, " Comparison of Kinetic Features Extracted in OSEM and FBP Reconstructed Dynamic PET Images for Oncology" *SNM Annual Conference 2000, San Louise, Mo., June 2000.*
3. X. Yu and C. C. Huang, "A Fast Method to Compute Covariance Matrix in Positron Emission Tomography Images", accepted by *IEEE Medical Imaging Conference 2000,* .
4. P. Thanyasrisung, X. Yu and C. C. Huang " Data Reduction for Fast Dynamic Positron-Emission Tomography (PET) Image Reconstruction and Lesion Detection" revised for a re-submission to *IEEE Tran. on Medical Image Processing.*
5. C. C. Huang, "Subspace Identification, Filtering and Identification with Applications to Lesion Detection in Dynamic PET Images", Ph. D. thesis in preparation to submit to USC Electrical Engineering Department, December 2000.

5 Conclusion

Our Year 1 effort is mainly concentrated on the physiological feature modeling and identification and the objective rank-reduction of dynamic PET sinogram for fast image reconstruction. Studying on the tasks for the following years has also been partially performed. The major accomplishments of this activity show the validity of applying the sophisticated subspace signal processing techniques, including subspace representation, identification, filtering and detection, to the detection of kinetic feature of axillary metastases in mathematics. The potential extension of the subspace parameter estimation from PET tomographic images to PET projection data, together with the newly developed technique for objective data reduction of dynamic PET projection data, makes it practical to detect breast cancer metastases with dynamic PET. All theoretical findings in Year 1 will be further tested and evaluated by a group of clinical patient data with proven primary breast cancer and palpable axillary metastases in Year 2. The mathematical models and algorithms will be validated with the results yielded from this group of patients with known lesions before applied to another group of patients with non-palpable axillary metastases in Year 3.

References

[1] D. Feng and X. Wang, "A computer simulation study on the effects of input function measurement noise in tracer kinetic modeling with positron emission tomography (PET)," *Comput. Bio. Med.,* Vol. 23, No. 1, p. 57-68, 1984.

[2] K. Schmidt, G. Mies, and L. Sokoloff, "Model of kinetic behavior of deoxyglucose in heterogeneous tissues in brain: A reinterpretation of the significant of parameters fitted to homogeneous tissue models," *J. Cerebral Blood Flow and Metabolism,* Vol. 11, p. 10-24, 1991.

[3] F. Osullivan, "Imaging radiotracer model parameters in PET: A mixture analysis approach", *IEEE Trans. on Medical Imaging*, Vol. 12, No. 3, pp. 399-412, 1993.

[4] K. S. Nijran and D. Barber, "Towards automatic analysis of dynamic radionuclide studies using principle-component factor analysis", *Phys. Med. Biol.*, 30, pp.1315-1325, December 1985.

[5] G. Blomqvist, "On the construction of functional maps in Positron emission tomorgraphy", *J Cereb Blood Flow Metab*, Vol. 4, 1984.

[6] R. E. Carson, S. C. Huang, M. V. Green, "Weighted integration methods for local cerebral blood flow measurements with positron emission tomography", *J Cereb Blood Flow Metab*, Vol. 6, 1986

[7] S. R. Meikle, J. C. Matthews, *et. al.*, "Spectral analysis of PET projection data", *IEEE Medical Imaing Conference Record*, pp. 1888 - 1892, 1997.

[8] M. N. Wernick, E. J. Infusino and C. M. Kao, "Fast optimal pre-reconstruction filters for dynamic PET," *IEEE MIC Conference,* 1997.

[9] C. M. Kao, J. T. Yap, J. Mukherjee and M. N. Wernick, "Image Reconstruction for Dynamic PET Based on Low-Order Approximation and Restoration of the Sinogram," *IEEE Trans. Medical Imaging,* Vol. 16, No. 6, Dec. 1997.

[10] C. C. Huang, X. Yu, J. Bading and P. S. Conti, "Feature extraction by subspace fitting of time activity curves in PET dynamic studies", *IEEE Medical Imaging Conference*, November 1997.

Appendix A: A Chapter of the Ph. D. Thesis (Draft) by C. C. Huang.

Chpater 2: Principles of Tracer Kinetic Modeling in PET

2.1 Overview

Tracer kinetic techniques are generally used in physiology and biochemistry to trace dynamic processes, such as blood flow, substrate transport, and biochemical reactions. By the application of the tracer kinetic method, PET can accurately estimate *in vivo* the tracer concentration, which provides functional and physiological variables, for example, the local cerebral metabolic rates of glucose (LCMRGlc) [52]. The tracer kinetic method involves a radiolabeled biologically active compound (tracer) and a mathematical model that describes the tracer kinetics during a biological process. Because FDG is useful in clinical PET for functional protocols (e.g., lesion detection, cardiology, neurology, oncology), the PET-FDG dynamic study will be focused in this dissertation.

For the tracer kinetic techniques, after being injected intravenously as a bolus, FDG concentration is measured to determine the transport rate constants of FDG in physiological compartmental models [34, 52, 59, 60]. The kinetic behavior of the tracer concentration in a tissue is called a time activity curve(TAC). From the physiological factor analysis (PFA), the tissue TAC in PET is modeled as a linear combination of the fundamental physiological functions which are called *basis* in signal processing. By using a mathematical 4-k compartmental model for a homogeneous tissue, each of the basis TAC functions can be represented as the exponential functions in time convolved with the arterial input function [36]. For a heterogeneous tissue containing a finite number of J overlapping independent homogeneous compartments, each of which is described by a physiological factor, the TAC will be represented as a weighted sum of the J independent physiological functions. The resulting physiologicial factos (using vector notation) define a subspace with dimension J embedded in a total N space [40].

2.2 Tracer Kinetic Techniques

In physiological studies, measurement of reactant and product chemical concentrations does not provide rates of a reaction sequence, because in vivo chemical concentrations can remain constant even though the rate of a process has changed. Furthermore, rates of disappearance or appearance of labeled reactants and products provide a means for measuring the rates and pathways of reaction sequences. The tracer kinetic techniques are among the most powerful methods for measuring the rates of processes for increasing knowledge of the biochemical, transport, and metabolism of body functions.

2.2.1 Principles of Tracer Kinetics

A small amount of detectable substrate (a tracer amount) can be introduced into fluid, and the speed of its passage through the system can be measured. The amount of label appearing in other chemical species will rise with some time delay and will later decrease gradually. From the amount of time delay, the rates of increase and decrease, and the concentration levels, the transport rates in a dynamic system can be estimated. However, the tracer kinetic techniques are more complicated in practical situations, e.g. the selection of tracers, the non-steady state condition, the mixture of inhomogeneous tissues, and the design of model for the dynamic process. Hence, it is necessary to design a tracer kinetic model to not only follow the dynamic process of interest, but also be mathematically tractable.

2.2.2 Tracer Kinetic Modeling: Development and Assumptions

For a tracer kinetic model [60] to approximate the real situations and to be mathematically manageable such that the solutions or analyses of the characteristics of the models are advantage .

A: Tracer selection
In tracer kinetic techniques, an appropriate tracer is required to follow the dynamic process of interest. Usually, a tracer must have the following properties:

- structurally related to the natural substance involved in the dynamic process (i.e., metabolic processes) or have similar transport properties (i.e., for flow system),
- measurable and distinguishable from the natural substance intended to be traced.

The well-known tracer used in PET is 2-[^{18}F]fluoro-2-deoxy-D-glucose (FDG), which has been used to isolate the transport and phosphorylation steps from the complicated pathway of glucose metabolism, thus enabling the formulation of simple tracer kinetic models for quantification of glucose utilization. DG is an analog of glucose in which the hydroxyl group on the number 2 carbon has been replaced with hydrogen. For PET this hydrogen is substituted for the positron emitter ^{18}F, forming FDG, Figure 1 [60]. DG and FDG have been used in biochemistry to isolate the phosphorylation reaction from the rest of glycolytic metabolism. FDG is transported into tissue and phosphorylated to FDG-6-phosphate (FDG-6-P) in the same manner as DG or glucose. However, because of the substitution in the second carbon position, FDG-6-P is not a substrate for the next reaction step in the metabolic pathway, Figure 2 [45]. FDG-6-P does not leave the cell except through a slow hydrolysis back to free FDG, which can then be transported to plasma or be rephosphorylated. Basically, FDG behaves similarly to glucose in its transport from plasma to tissue and in its

phosphorylation, the rate of which, under a steady-state condition for glucose, is equal to the utilization rate of exogenous glucose. Therefore, the utilization rate of glucose is predictable from the kinetics of FDG.

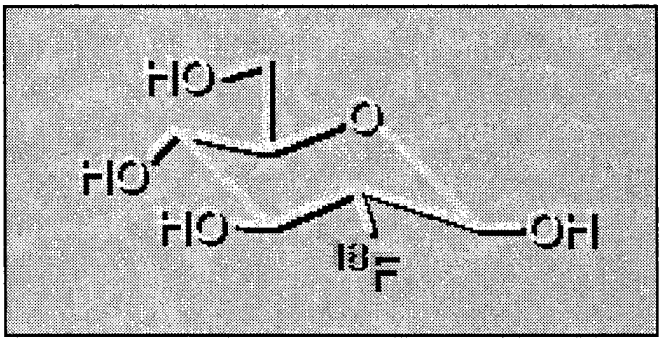

Figure 1: FDG structure.

Although there are a variety of tracers for PET cancer imaging, the most useful is based on the increasing use of glucose by tumor cells. FDG is a structural analogue of 2-deoxyglucose which is D-glucose without an OH group in the 2-position [63]. Because of this structural alteration, 2-deoxyglucose is transported into the cancer cell like glucose, and, is phosphorylated by hexokinase. This phosphorylation to 2-DG-6phosphate results in a polar intermediate which does not cross cell membranes well, i.e., it is trapped in cancer cells. 2-DG can be dephosphorylated to 2DG by glucose-6-phosphatase, but this reaction occurs slowly, particularly in cancer cells, which commonly lack glucose-6-phosphatase. ^{18}F attached to the 2-position of this molecule results in FDG, which behaves in a similar fashion to 2-DG, but the ^{18}F emits positrons, the decay of which can be imaged.

FDG uptake for a variety of human cancers has been shown to have high tumor-background uptake ratios at 1-2 hour post i.v. injection [?, 64]. The mechanisms for this increased FDG-6-phosphate accumulation in many cancer cells has been shown to be due to [65]:

- increased expression of glucose transporter molecules at the tumor cell surface
- increased activity of hexokinase
- reduced levels of glucose-6-phosphatase v.s. most normal tissues.

The property that cancer cells avidly accumulate FDG-6-phosphate is important for lesion detection and is fundamental to the method introduced in this

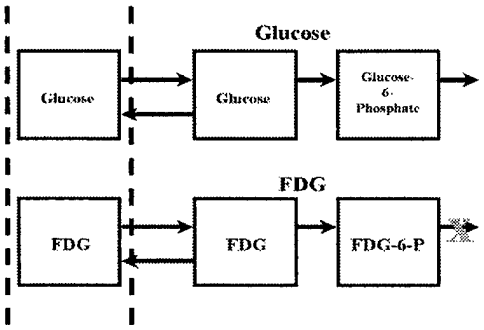

(a)

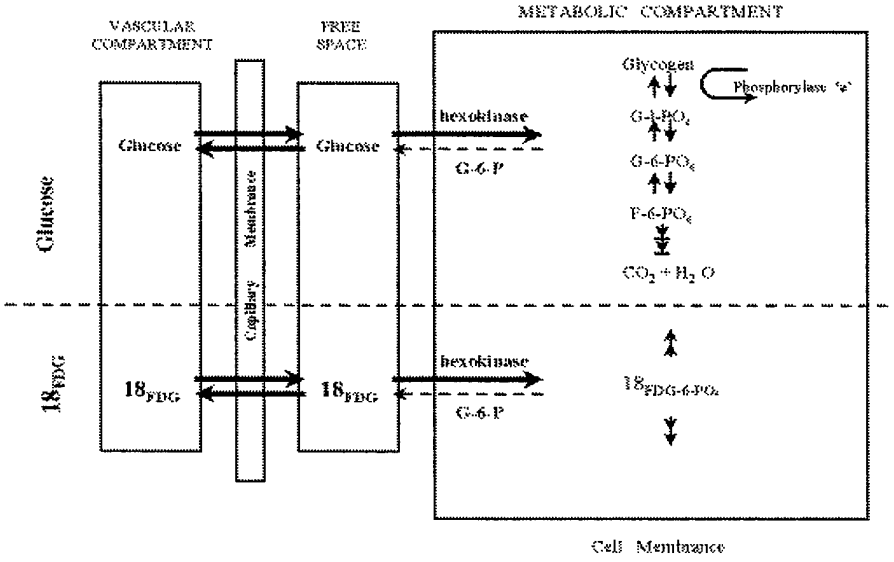

(b)

Figure 2: The transport and metabolic reaction pathways of FDG compared with glucose in tissue. (a) FDG is transported in tissue and phosphorylated to FDG-6-P in the same manner as glucose, (b) FDG-6-P is not a substrate for the reaction step in the metabolic compartment.

dissertation.

B: Model selection

Mathematical models are often applied to incorporate the *a priori* information about a process (such as biochemical sequence, membranes that must be crossed) and to restrict the representation of the tracer kinetic behavior to a limited set of functions in order to allow the interpretation of measurements. For tracer kinetics, there exists various types of mathematical models of widely different mathematical characteristics, such as deterministic versus stochastic, distributed versus non-distributed, compartmental versus non-compartmental, and linear versus nonlinear. In biochemical applications (e.g., PET), linear compartmental models are most frequently used, because of their advantageous mathematical properties that enable straightforward solution or analysis of the model characteristics.

- Compartmental Model
  A compartmental model (Figure ??compart) is usually represented by a number of compartments connected by a number of arrows indicating transport between compartments. A compartment is defined as a space in which the tracer is distributed uniformly. The amount of tracer leaving a compartment is assumed to be proportional to the total amount in the compartment. The arrows indicate the possible pathways the tracer can follow. The symbol k, the rate constant with the unit of inverse time, denotes the fraction of the total tracer that would leave the compartment per unit time.

- Linear Model
  Generally, not many physiological processes or biochemical reactions can be considered to be linear. However, linearity is usually valid for tracer transport or chemical reactions given that the amount of tracer is always very small compared with its natural counterpart, which has a constant concentration. Because of this linearity property of the tracer, the kinetics of a physiological or biochemical process can be completely represented by a response function (system function). The response function of a system will be exactly the tracer kinetics measurements from the system, if the tracer is delivered to the system as an impulse (i.e., as a short bolus with no recirculation).

Based on the linear compartmental model assumption, the tracer kinetics of a compartmental model can be described in terms of a set of linear, first-order, constant-coefficient, ordinary differential equations. If certain conditions are fulfilled, e.g., initial conditions are zero, the solutions to the differential equations will simply be the convolution of the delivery function (input function) and the response function of the system. The response function of a compartmental model will consist of a sum of exponential functions. Usually, the number of ex-

ponential components is equal to the number of compartments in the model. If the input function (i.e., arterial blood or plasma time-activity curve) is known, the response function of the system can be deduced by deconvolving the input function from the measured kinetics of the system. Thus, by analyzing the response function in terms of exponential components, one can estimate the number of compartments required for constructing a system model. The fact that the response functions of many biological or physiological systems can be decomposed into a sum of exponential components is another indication that the compartmental models are adequate for tracer kinetics studies.

C: Assumptions in the tracer kinetic modeling

In tracer kinetic modeling, the followings are usually assumed in order for the model to have tractable mathematical properties:

- The tracer introduced is assumed to be in a trace amount, so that the measured results would reflect the effect of the tracer introduction and not represent the original process.

- The dynamic process for tracer kinetics is assumed to be in a steady state. That is, the rate of transport or reaction of the system is unchanged with time, and the amount of substance in any part of the system is constant during the evaluation time. For practical systems, because biological systems continuously change to adapt the environment, there is no absolute steady state. However, the steady state condition is considered to be sufficient if the amount of change within the time of evaluation is minor compared to the magnitude of the process itself. For example, the FDG method for the measurement of glucose utilization requires a study period of about 45 minutes or longer, during which the glucose utilization rate in tissue may change.

- The contribution of different tissues to a tracer kinetic measurement is another unavoidable practical problem. With the advantage of PET, the concentration of positron-emitting in small local regions of the body can be not only quantitatively measured, but also anatomically differentiated to a significant degree. With the use of radiotracers and scintillation detectors (individual detectors and scintillation cameras), the concentration of positron-emission radioactivity in small local regions of the body can be quantitatively measured with PET scanners. This capability has a large impact on the tracer kinetic model, such that not only can the absolute tracer concentration in tissue be obtained, but also anatomically heterogeneous tissues can be delineated to a significant degree. Hence, tracer kinetics measured from a small tissue element can be more accurately modeled as a homogeneous uniform pool. As far as the transport of tracer is concerned, the only connection between a small tissue element and other parts of the organ or body is the tracer delivery and clearance

through the blood flow in the tissue element. Therefore, the tracer concentration in the supplying blood that can be measured from peripheral arterial blood samples or an ROI data drawn inside a PET heart images can be considered as the input function to the tracer kinetic system in the small tissue element. Hence, a small tissue element can be reasonably regarded as a homogeneous uniform pool.

- As far as the transport of tracer is concerned, the only connection between a small tissue element and other parts of the organ is the tracer delivery and clearance through the blood flow in the tissue element. Therefore, the tracer concentration in the supplying blood that can be measured from the arterial blood samples can be considered as the input function to the tracer kinetic system in the small tissue element.

2.2.3 4-k Compartmental Model for the FDG Tracer Kinetics

A: Homogeneous Tissues

The subject of a PET-FDG dynamic study, under homogeneous tissue type, could be considered as a plasma compartment and a tissue compartment. At the beginning of a PET-FDG dynamic study, FDG is absent in both plasma compartment and tissue compartment. Following a bolus injection into the plasma, the FDG concentration would initially peak in the plasma compartment and later peak in the tissue compartment after FDG enters the tissue and is phosphorylated into FDG-6-phosphate (FDG-6-P). Because of the missing oxygen at the second carbon position, FDG-6-P can not be further metabolized in the metabolic pathway. The transfer of FDG from the plasma compartment to the tissue compartment is shown in Figure 3. The most common type of models for describing the FDG transfer are linear compartmental models, in which rate constants describe the rate of exchange of tracer between discrete compartments. Figure 3 shows a 4k compartmental model for FDG, where the compartments represent FDG in plasma, FDG in tissue, and phosphorylated FDG in tissue (FDG-6-P). Phosphorylation of FDG is mediated by the hexokinase enzyme and, unlike glucose, is the terminal reaction step. The fact that FDG does not continue to be metabolized through the glycolytic pathway is an advantage for modeling purposes because the number of rate constants are manageable. The rate constants in Figure 3 are defined as follows:

$$
\begin{aligned}
K_1^* &= \text{the transport of FDG in plasma to tissue} \\
k_2^* &= \text{the transport of FDG in tissue to plasma} \\
k_3^* &= \text{the phosphorylation of FDG to FDG-6-P} \\
k_4^* &= \text{the dephosphorylation of FDG-6-P to FDG.}
\end{aligned}
$$

The following first-order, constant-coefficient, ordinary differential equations describe the rate of change in the concentrations of FDG and FDG-6-P in a ho-

mogeneous tissue:

$$\begin{aligned}\frac{dC_e^*(t)}{dt} &= K_1^* C_p^*(t) - (k_2^* + k_3^*)C_e^*(t) + k_4^* C_m^*(t) \\ \frac{dC_m^*(t)}{dt} &= k_3^* C_e^*(t) - k_4^* C_m^*(t), \end{aligned} \tag{1}$$

where $*$ indicates decay-corrected FDG tracer quantities, $C_e^*(t)$ represents the concentration of FDG in the tissue at time t, $C_m^*(t)$ represents the concentration of FDG-6-P (and all metabolites derived from FDG-6-P) in the same region, and $C_p^*(t)$ represents the FDG concentration in the arterial plasma. Solutions of (1) [52] given that the initial conditions $C_e^*(0) = C_m^*(0) = 0$ show that the total radioactivity for a homogeneous tissue, $C^*(t)$, is the sum of the free [^{18}F]FDG concentration plus the concentration of metabolites, i.e.,

$$\begin{aligned} C^*(t) &= C_e^*(t) + C_m^*(t) \\ &= \frac{K_1^*}{\alpha_2 - \alpha_1}\left[(k_3^* + k_4^* - \alpha_1)\mathrm{e}^{-\alpha_1 t} + (\alpha_2 - k_3^* - k_4^*)\mathrm{e}^{-\alpha_2 t}\right] \otimes C_p^*(t) \\ &= \left[M_1 \mathrm{e}^{-\alpha_1 t} + M_2 \mathrm{e}^{-\alpha_2 t}\right] \circledcirc C_p^*(t), \end{aligned} \tag{2}$$

where

$$\begin{aligned} \alpha_1 &= \frac{1}{2}\left[(k_2^* + k_3^* + k_4^*) - \sqrt{(k_2^* + k_3^* + k_4^*)^2 - 4k_2^* k_4^*}\right] \\ \alpha_2 &= \frac{1}{2}\left[(k_2^* + k_3^* + k_4^*) + \sqrt{(k_2^* + k_3^* + k_4^*)^2 - 4k_2^* k_4^*}\right] \\ M_1 &\triangleq \frac{K_1^*}{\alpha_2 - \alpha_1}(k_3^* + k_4^* - \alpha_1) \\ M_2 &\triangleq \frac{K_1^*}{\alpha_2 - \alpha_1}(\alpha_2 - k_3^* - k_4^*) \end{aligned} \tag{3}$$

and $\circledcirc$ denotes the convolution operator.

The radioactivity measured by the PET scanner (under noise-free assumption), including the radioactivity in the cerebral blood, can be represented as

$$\begin{aligned} C_{\text{total}}^*(t) &= V_b C_p^*(t) + C^*(t) \\ &= V_b C_p^*(t) + \left[M_1 \mathrm{e}^{-\alpha_1 t} + M_2 \mathrm{e}^{-\alpha_2 t}\right] \circledcirc C_p^*(t), \end{aligned} \tag{4}$$

where $C_{\text{total}}^*(t)$ is the total radioactivity measured by the scanner at time t; V_b denotes the vascular space in tissue and FDG concentration in whole blood is assumed to be $V_b C_p^*(t)$ at time t [45].

In order to characterize the complex behaviors of the realistic plasma TAC, such as the period of zero activity at the beginning due to delay from tracer delivery, the rapidly rising period, and the exponential-like decay period, Feng and Wang [16] used a compartmentalized model to represent tracer behavior

Figure 3: A 4-k compartmental model

in the blood circulatory system,where The FDG plasma TAC was represented by a 4th-order exponential curve with a pure decay and a pair of repeated eigenvalues:

$$C_p^*(t) = \{[B_1(t-\tau) - B_2 - B_3]\,\mathrm{e}^{-\lambda_1(t-\tau)} + B_2\mathrm{e}^{-\lambda_2(t-\tau)} + B_3\mathrm{e}^{-\lambda_3(t-\tau)}\}\,1(t-\tau), \tag{5}$$

where λ_1, λ_2, and λ_3 are the eigenvalues of the blood circulatory system (1/min); B_1, B_2, and B_3 are the coefficients (μCi/ml); τ is the delay constant (min); and

$$1(t-\tau) \triangleq \begin{cases} 0, & \text{if } t < \tau \\ 1, & \text{if } t \geq \tau. \end{cases} \tag{6}$$

A substitution of Eq. (5), assuming τ to be 0, into Eq. (4) yields $C_{\text{total}}^*(t)$ as

$$C_{\text{total}}^*(t) = E_1 t\mathrm{e}^{-\lambda_1 t} + E_2\mathrm{e}^{-\lambda_1 t} + E_3\mathrm{e}^{-\lambda_2 t} + E_4\mathrm{e}^{-\lambda_3 t} + E_5\mathrm{e}^{-\alpha_1 t} + E_6\mathrm{e}^{-\alpha_2 t}, \tag{7}$$

where

$$\begin{aligned}
E_1 &\triangleq V_b B_1 + \frac{M_1 B_1}{-(\lambda_1 - \alpha_1)} + \frac{M_2 B_1}{-(\lambda_1 - \alpha_2)} \\
E_2 &\triangleq -V_b(B_2 + B_3) + \left[\frac{-M_1 B_1}{(\lambda_1 - \alpha_1)^2} + \frac{M_1(B_2 + B_3)}{\lambda_1 - \alpha_1}\right] + \left[\frac{-M_2 B_1}{(\lambda_1 - \alpha_2)^2} + \frac{M_2(B_2 + B_3)}{\lambda_1 - \alpha_2}\right] \\
E_3 &\triangleq V_b B_2 + \frac{M_1 B_2}{-(\lambda_2 - \alpha_1)} + \frac{M_2 B_2}{-(\lambda_2 - \alpha_2)} \\
E_4 &\triangleq V_b B_3 + \frac{M_1 B_3}{-(\lambda_3 - \alpha_1)} + \frac{M_2 B_3}{-(\lambda_3 - \alpha_2)} \\
E_5 &\triangleq \frac{M_1 B_1}{(\lambda_1 - \alpha_1)^2} + \frac{M_1(B_2 + B_3)}{-(\lambda_1 - \alpha_1)} + \frac{M_1 B_2}{\lambda_2 - \alpha_1} + \frac{M_1 B_3}{\lambda_3 - \alpha_1} \\
E_6 &\triangleq \frac{M_2 B_1}{(\lambda_1 - \alpha_2)^2} + \frac{M_2(B_2 + B_3)}{-(\lambda_1 - \alpha_2)} + \frac{M_2 B_2}{\lambda_2 - \alpha_2} + \frac{M_2 B_3}{\lambda_3 - \alpha_2}.
\end{aligned} \tag{8}$$

For $t = t_1, \cdots, t_N$, N is the number of frames, the radioactivity, $C^*_{\text{total}}(t_n)$, $n = 1, \cdots, N$, for the homogeneous tissue can be represented as a column vector

$$\mathbf{c}_{\text{homo}} = \mathbf{\Gamma}_p \mathbf{a}_p + \mathbf{\Gamma}_{tissue} \mathbf{a}_{tissue}, \tag{9}$$

where

$$\begin{aligned}
\mathbf{\Gamma}_p &\triangleq \begin{bmatrix} t_1 e^{-\lambda_1 t_1} & e^{-\lambda_1 t_1} & e^{-\lambda_2 t_1} & e^{-\lambda_3 t_1} \\ t_2 e^{-\lambda_1 t_2} & e^{-\lambda_1 t_2} & e^{-\lambda_2 t_2} & e^{-\lambda_3 t_2} \\ \vdots & \vdots & \vdots & \vdots \\ t_N e^{-\lambda_1 t_N} & e^{-\lambda_1 t_N} & e^{-\lambda_2 t_N} & e^{-\lambda_3 t_N} \end{bmatrix}, \\
\mathbf{\Gamma}_{tissue} &\triangleq \begin{bmatrix} e^{-\alpha_{11} t_1} & e^{-\alpha_{12} t_1} \\ e^{-\alpha_{11} t_2} & e^{-\alpha_{12} t_2} \\ \vdots & \vdots \\ e^{-\alpha_{11} t_N} & e^{-\alpha_{12} t_N} \end{bmatrix}, \\
\mathbf{a}_p &\triangleq [E_1, E_2, E_3, E_4]^T, \quad \mathbf{a}_{tissue} \triangleq [E_5, E_6]^T.
\end{aligned} \tag{10}$$

B: Heterogeneous Tissues

Due to the limited spatial resolution of the PET scanner and the forward and backward processes in a PET system, measurement of radioactivity in a homogeneous tissue is rarely, if ever achieved. For such reason, the mixture analysis or the physiological factor analysis (PFA) was used to incorporate the heterogeneity effects for a heterogeneous region of interest, where the mixed tissue TAC can be represented as the mass-weighted average of physiological function in each of the finite homogeneous tissues [?, 34, 51, 42]. For a mixed (heterogeneous) tissue pixel containing a finite number of J overlapping independent homogeneous compartments, each of which is described by a physiological factor, the TAC will be represented as a weighted sum of the J independent physiological functions. The physiologicial factos (using vector notation) define a subspace with dimension J embedded in a total N space.

Hence, given that a mixed (heterogeneous) tissue pixel contains J homogeneous subregions with the radioactivity in each subregion j described by, from Eq. (2),

$$\begin{aligned}
C^*_j(t) &= C^*_{ej}(t) + C^*_{mj}(t) \\
&= \frac{K^*_{1j}}{\alpha_{2j} - \alpha_{1j}} \left[(k^*_{3j} + k^*_{4j} - \alpha_{1j}) e^{-\alpha_{1j} t} - (\alpha_{2j} - k^*_{3j} - k^*_{4j}) e^{-\alpha_{2j} t} \right] \otimes C^*_p(t),
\end{aligned} \tag{11}$$

then $\bar{C}^*(t)$, the weighted average radioactivity in a heterogeneous tissue, can be written as

$$\bar{C}^*(t) = \sum_{j=1}^{J} w_j C^*_j(t)$$

$$= \sum_{j=1}^{J} \frac{w_j K_{1j}^*}{\alpha_{2j} - \alpha_{1j}} \left[(k_{3j}^* + k_{4j}^* - \alpha_{1j}) e^{-\alpha_{1j} t} + (\alpha_{2j} - k_{3j}^* - k_{4j}^*) e^{-\alpha_{2j} t} \right] \otimes C_p^*(t),$$

$$= \sum_{j=1}^{J} w_j [M_{1j} e^{-\alpha_{1j} t} + M_{2j} e^{-\alpha_{2j} t}] \otimes C_p^*(t), \tag{12}$$

where w_j is the weighting coefficient for the jth homogeneous subregion; $M_{1j} \triangleq \frac{K_{1j}^*}{\alpha_{2j} - \alpha_{1j}} (k_{3j}^* + k_{4j}^* - \alpha_{1j})$ and $M_{2j} \triangleq \frac{K_{1j}^*}{\alpha_{2j} - \alpha_{1j}} (\alpha_{2j} - k_{3j}^* - k_{4j}^*)$; the variables K_{1j}, k_{2j}, k_{3j}, k_{4j}, α_{1j}, and α_{2j} for the jth subregion in a heterogeneous tissue have the same physiological meanings for those defined in the homogeneous tissue case. Eq. (12) is the equation widely used in the spectral analysis of PET dynamic studies [15, 36], where the tissue TAC is modeled as a convolution of the measured plasma or input function with a sum of $2J$ exponential terms:

$$\bar{C}^*(t) = \sum_{i=1}^{2J} \gamma_i e^{-\beta_i t} \otimes C_p^*(t), \tag{13}$$

where γ_i depends on w_j, M_{1j}, and M_{2j}; $\{\alpha_{1j}, \alpha_{2j} | j = 1, \cdots, J\} = \{\beta_i | i = 1, \cdots, 2J\}$.

A use of the plasma function in Eq. (5) results $C_{\text{total}}^*(t)$ in the following:

$$\begin{aligned} \bar{C}_{\text{total}}^*(t) &= V_b C_p^*(t) + \bar{C}^*(t) \\ &= V_b C_p^*(t) + \sum_{j=1}^{J} w_j [M_{1j} e^{-\alpha_{1j} t} + M_{2j} e^{-\alpha_{2j} t}] \otimes C_p^*(t) \\ &= \bar{E}_1 t e^{-\lambda_1 t} + \bar{E}_2 e^{-\lambda_1 t} + \bar{E}_3 e^{-\lambda_2 t} + \bar{E}_4 e^{-\lambda_3 t} + \sum_{j=1}^{J} w_j E_{5j} e^{-\alpha_{1j} t} + \sum_{j=1}^{J} w_j E_{6j} e^{-\alpha_{2j} t}, \end{aligned} \tag{14}$$

where

$$\begin{aligned} \bar{E}_1 &\triangleq V_b B_1 + \sum_{j=1}^{J} w_j \left[\frac{M_{1j} B_1}{-(\lambda_1 - \alpha_{1j})} + \frac{M_{2j} B_1}{-(\lambda_1 - \alpha_{2j})} \right] \\ \bar{E}_2 &\triangleq -V_b (B_2 + B_3) + \sum_{j=1}^{J} w_j \left\{ \left[\frac{-M_{1j} B_1}{(\lambda_1 - \alpha_{1j})^2} + \frac{M_{1j} (B_2 + B_3)}{\lambda_1 - \alpha_{1j}} \right] + \right. \\ &\quad \left. \left[\frac{-M_{2j} B_1}{(\lambda_1 - \alpha_{2j})^2} + \frac{M_{2j} (B_2 + B_3)}{\lambda_1 - \alpha_{2j}} \right] \right\} \\ \bar{E}_3 &\triangleq V_b B_2 + \sum_{j=1}^{J} w_j \left[\frac{M_{1j} B_2}{-(\lambda_2 - \alpha_{1j})} + \frac{M_{2j} B_2}{-(\lambda_2 - \alpha_{2j})} \right] \end{aligned}$$

$$
\begin{aligned}
\bar{E}_4 &\triangleq V_b B_3 + \sum_{j=1}^{J} w_j \left[\frac{M_{1j} B_3}{-(\lambda_3 - \alpha_{1j})} + \frac{M_{2j} B_3}{-(\lambda_3 - \alpha_{2j})} \right] \\
E_{5j} &\triangleq \frac{M_{1j} B_1}{(\lambda_1 - \alpha_{1j})^2} + \frac{M_{1j}(B_2 + B_3)}{-(\lambda_1 - \alpha_{1j})} + \frac{M_{1j} B_2}{\lambda_2 - \alpha_{1j}} + \frac{M_{1j} B_3}{\lambda_3 - \alpha_{1j}} \\
E_{6j} &\triangleq \frac{M_{2j} B_1}{(\lambda_1 - \alpha_{2j})^2} + \frac{M_{2j}(B_2 + B_3)}{-(\lambda_1 - \alpha_{2j})} + \frac{M_{2j} B_2}{\lambda_2 - \alpha_{2j}} + \frac{M_{2j} B_3}{\lambda_3 - \alpha_{2j}}.
\end{aligned} \tag{15}
$$

The weighted average radioactivity, $\bar{C}^{*}_{\text{total}}(t_n)$, $n = 1, \cdots, N$, for the heterogeneous tissue can be represented as a column vector

$$
\mathbf{c}_{\text{hetero}} = \mathbf{\Gamma}_p \tilde{\mathbf{a}}_p + \tilde{\mathbf{\Gamma}}_{tissue} \tilde{\mathbf{a}}_{tissue}, \tag{16}
$$

where

$$
\begin{aligned}
\tilde{\mathbf{\Gamma}}_{tissue} &\triangleq \begin{bmatrix}
e^{-\alpha_{11} t_1} & e^{-\alpha_{12} t_1} & \cdots & e^{-\alpha_{1J} t_1} & e^{-\alpha_{21} t_1} & e^{-\alpha_{22} t_1} & \cdots & e^{-\alpha_{2J} t_1} \\
e^{-\alpha_{11} t_2} & e^{-\alpha_{12} t_2} & \cdots & e^{-\alpha_{1J} t_2} & e^{-\alpha_{21} t_2} & e^{-\alpha_{22} t_2} & \cdots & e^{-\alpha_{2J} t_2} \\
\vdots & \vdots & \cdots & \vdots & \vdots & \vdots & \vdots & \vdots \\
e^{-\alpha_{11} t_N} & e^{-\alpha_{12} t_N} & \cdots & e^{-\alpha_{1J} t_N} & e^{-\alpha_{21} t_N} & e^{-\alpha_{22} t_N} & \cdots & e^{-\alpha_{2J} t_N}
\end{bmatrix}_{N \times 2J} \\
\tilde{\mathbf{a}}_p &\triangleq [\bar{E}_1, \bar{E}_2, \mathbf{E}_3, \mathbf{E}_4]^T \\
\tilde{\mathbf{a}}_{tissue} &\triangleq [E_{51}, E_{52}, \cdots, E_{5J}, E_{61}\ E_{62}, \cdots, E_{6J}]^T,
\end{aligned} \tag{17}
$$

and $\mathbf{\Gamma}_p$ is defined in Eq. (10).

References

[1] L. P. Adler, J. P. Crowe, N. K. Al-kaisi, *et al.*, "Evaluation of breast masses and axillary lymph nodes with [F-18] 2-Deoxy-2-fluoro-D-glucose PET," *Radiology.* 187: p. 743-750, 1993.

[2] J. Aliresaie, C. Nahmias, and M. E. Jernigan, "Neural network based segmentation of magnetic resonance images of the brain," *IEEE Nuclear Science Symposium,* 3: p. 1397-1401, 1995.

[3] N. M. Alpert, *et al.*, "Estimation of the local statistical noise in emission computed tomography," *IEEE Transactions on Medical Imaging,* Vol. MI-1, No. 2, p. 142-146, Oct. 1982.

[4] S. C. Amartur, D. Piraino, and Y. Takefuji, "Optimization neural networks for the segmentation of magnetic resonance images," *IEEE on Transactions on Medical Imaging.* Vol. 11, No. 2, p. 215-220, 1992.

[5] D. Barber, "The use of principal components in the quantitative analysis of gamma camera dynamic studies," *Phys. Med. Biol.,* 25: p. 283-292, 1980.

[6] R. T. Behrens and L. L. Scharf, "Signal processing applications of oblique projection operators," *IEEE Transactions on Signal Processing,* Vol. 42, No. 6, p. 1413-1424, June 1994.

[7] R. E. Carson, *et al.*, "An approximation formula for the variance of PET region-of-interest values," *IEEE Transactions on Medical Imaging,* Vol. 12, No. 2, p. 240-250, June 1993.

[8] S. R. Cherry and M. E. Phelp. Imaging brain function with positron emission tomography. In Arthur W. Toga and John C. Mazziotta, editors, "Brain Mapping: The Methods," Chapter 8. Academic Press, 1996.

[9] H. S. Choi, D. R. Haynor, and Y. Kim, "Partial volume tissue classification of multichannel magnetic resonance images - A mixed model," *IEEE Transactions on Medical Imaging,* Vol. 10, No. 3, Sep. 1991.

[10] P. S. Conti, *et al.,* "Carbon-11 labeled alpha-aminoisobutyric acid, 2-deoxy-D-glucose and thymidine as potential imaging agents for prostatic and renal malignancies," *Surgical Form,* Vol. 36, p. 635-637, 1985.

[11] P. S. Conti, *et al.*, "Multiple radiotracers for evaluation of intracranial mass lesion using PET," *Journal of Nuclear Medicine,* Vol. 32, p. 954-970, 1991.

[12] P. S. Conti *et al.*, "PET and [^{18}F]-FDG in oncology: a clinical update," *Nuclear Medicine and Bio.*, Vol: 23, p. 717-735, 1996.

[13] Thomas M. Cover, "An algorithm for maximizing expected log investment return," *IEEE Transactions Info. Theory*, Vol. IT-30, No. 2, p. 369-373, March 1984.

[14] L. P. Crowe, L. P. Adler, R. R. Shenk, and J. Sunshine, "Positron emission tomography and breast masses: comparison with clinical, mammographic, and pathological findings," *Annals Surg Oncol.*, Vol. 1, p. 132-140, 1994.

[15] V. J. Cunningham and T. Jones "Spectral analysis of dynamic PET studies," *Journal Cerebral Blood Flow and Metabolism*, 13:15-23, 1993.

[16] D. Feng and X. Wang, "A computer simulation study on the effects of input function measurement noise in tracer kinetic modeling with positron emission tomography (PET)," *Comput. Bio. Med.*, Vol. 23, No. 1, p. 57-68, 1984.

[17] R. H. Huesman, "A new fast algorithm for the evaluation of regions of interest and statistical uncertainty in computed tomography," *Phys. Med. Biol.*, Vol. 29, No. 5, p. 543-552, 1984.

[18] E. Ü. Mumcuoğlu, R. M. Leahy, S. R. Cherry, and Z. Zhou, "Fast gradient-based methods for Bayesian reconstruction of transmission and emission PET images," *IEEE Transactions on Medical Imaging*, Vol. 13, No. 4, p. 687-701, Dec. 1994.

[19] E. Ü. Mumcuoğlu, R. M. Leahy, and S. R. Cherry, "Bayesian reconstruction of PET images: methodology and performance analysis," *Phys. Med. Biol.*, Vol. 41, No. 9, p. 1777-1807, Sep. 1996.

[20] J. A. Fessler, "Mean and variance of implicitly defined biased estimators (such as penalized maximum likelihood): application to tomography," *IEEE Transactions on Image Processing*, Aug. 1995.

[21] G. H. Golub and C. F. Van Loan, *Matrix Computation*, 3rd edition, the Johns Hopkins University Press, 1996.

[22] G. L. Brownell, T. F. Budinger, P. C. Lauterbur, and P. L. McGeer, "Positron tomography and nuclear magnetic resonance imaging," *Science*, p. 619-626, Feb. 1982.

[23] P. J. Green, "Bayesian reconstruction from emission tomography data using a modified EM algorithm," *IEEE Transactions on Medical Imaging*, Vol. MI-9, No. 1, p. 84-93, Mar. 1990.

[24] T. J. Hebert and R. M. Leahy, "A generalized EM algorithm for 3-D Bayesian reconstruction from Poisson data using Gibbs priors," *IEEE Transactions on Medical Imaging*, Vol. MI-8, No. 2, p. 194-202, June 1989.

[25] H. M. Hudson and R. S. Larkin "Accelerated image reconstruction using ordered subsets of projection data," *IEEE Transactions on Medical Imaging*, 1994.

[26] C. C. Huang and X. Yu, "Computer-aided lesion detection with statistical model-based features in PET images," *USC-Radiology Internal Report*, July, 1996.

[27] C. C. Huang, X. Yu, J. Zheng, J. R. Bading, and P. S. Conti, "Algorithm to reduce the complexity of local statistics computation for PET images," *SPIE Proceeding on Medical Imaging*, Vol. 3034, p. 1094-1111, Newport Beach, CA, Feb. 1997.

[28] C. C. Huang, X. Yu, J. R. Bading, and P. S. Conti, "Computer-aided lesion detection with statistical model-based features in PET images," *IEEE Transactions on Nuclear Science*, Vol. 44, No. 6, p. 2509-2521, Dec. 1997.

[29] C. C. Huang, X. Yu, J. Bading, and P. S. Conti, "Feature extraction by subspace fitting of time activity curve in PET dynamic studies," *IEEE Medical Image Conference*, Nov. 1997.

[30] R. H. Huesman, "A new fast algorithm for the evaluation of regions of interest and statistical uncertainty in computed tomography," *Phys. Med. Biol.*, Vol. 29, No 5, p. 543-552, 1984.

[31] A. C. Kak and M. Slaney, *Principles of Computerized Tomography Imaging*, IEEE Press, 1987.

[32] K. Kubota, T. Matsuzawa, *etc.*, "Differential diagnosis of lung tumor with positron emission tomography: A prospective study," *Journal of Nuclw Medicine*, Vol. 31, p. 1927-1933, 1990.

[33] J. Llacer, *et al.*, "Results of a clinical receiver operating characteristic study comparing filtered backprojection and maximum likelihood estimator images in FDG PET studies," *Journal of Nuclear Medicine*, Vol. 34, p. 1198-1203, 1993.

[34] G. Lucignani, K. C. Schmidt, R. M. Moreco, *et al.*, "Measurement of regional cerebral glucose utilization with Fluorine-18-FDG and PET in heterogeneous tissues: Theoretical considerations and practical procedure," *Journal Nuclear Medicine*, Vol. 34, No, 3, 360-369, Mar. 1993.

[35] S. R. Meikle and M. Dahlbom "Positron emission tomography: application in oncology" *Nuclear Medicine in Clinical Diagnosis and Treatment*, edited by I. P. C. Murray and P. J. Ell, Vol. 2, p. 1327-1337.

[36] S. R. Meikle, J. C. Matthews, V. J. Cunningham, *etc.* "Spectral analysis of PET projection data," *Medical Imaging Conference,* p. 1888-1892, 1997.

[37] C. E. Metz, "Basic principles of ROC analysis," *Semin. Nuclear Medicine,* Vol. 4, p. 283-298, 1978.

[38] Michel M. Ter-Pogossian, Marcus E. Raichle, and Burton E. Sobel, "Positron-Emission Tomography," *Scientific American,* 243 (4), p. 171-181, 1980.

[39] K. S. Nijran and D. Barber, "Towards automatic analysis of dynamic radionuclide studies using principal-component factor analysis," *Phys. Med. Biol.,* 30: p. 1315-1325, Dec. 1985.

[40] K. S. Nijran and D. Barber, "Factor analysis of dynamic function studies using a priori physiological information," *Phys. Med. Biol.,* 31: p. 1107-1117, Oct. 1986.

[41] D. Ortendahl, "The application of principal component analysis to multivariate MRI data," *Proceeding of the 8th annual conference of the engineering in medical and biology society,* Fort Worth, Texas 1986: p. 1065-1068.

[42] Finbarr O'Sullivan, "Imaging radiotracer model parameters in PET: A Mixture analysis approach," *IEEE Transaction Medical Imaging* Vol. 12, No. 3, p. 399-412, 1993.

[43] R. Maitra and F. O'Sullivan, "Estimating the variability of reconstructed PET data: a technique based on approximating the reconstruction filter by a sum of Gaussian kernels," *IEEE Nuclear Science Symposium,* Vol. 3, p. 1411-1414, 1995.

[44] F. Pedersen, M. Bergstrom, E. Bengtsson, and B. Langstrom, "Principal component analysis of dynamic positron emission tomography images," *European Journal of Nuclear Medicine,* Vol. 21, No. 12, p. 1285-1292, Dec. 1994.

[45] M. E. Phelps, J. C. Mazziotta, and H. R. Schelbert, *Positron Emission Tomography and Autoradiology, Principles and Applications for the Brain and Heart,* Raven Press, 1986.

[46] I. S. Reed and X. Yu, "Adaptive multi-band CFAR detection of an optical pattern with unknown spectral distribution," *IEEE Transactions on Acoustic, Speech, and Signal Processing,* Vol. 38, No. 10, (pages?), Oct. 1990.

[47] P. Santago, and H. D. Gage, "Quantification of MR brain images by mixture density and partial volume modeling," *IEEE Transactions on Medical Imaging*, Vol. 12, No. 3, Sep. 1993.

[48] L. L. Scharf, *Statistical Signal Processing*. MA: Addison-Wesley, 1991.

[49] L. L. Scharf and B. Friedlander, "Matched subspace detectors," *IEEE Transactions on Signal Processing*, Vol. 42, No. 8, p. 2146-2157, Aug. 1994.

[50] B. Schmall, P. S. Conti, D. J. Schaeffer, and E. L. Kleinert, "Tumor and organ biochemical profiles determined in vivo following uptake of a combination of radiolabeled substrates: potential applications for PET," *Amer. Journal Phys. Imag.*, Vol. 7, p. 2-11, 1992.

[51] K. Schmidt, G. Mies, and L. Sokoloff, "Model of kinetic behavior of deoxyglucose in heterogeneous tissues in brain: A reinterpretation of the significant of parameters fitted to homogeneous tissue models," *Journal Cerebral Blood Flow and Metabolism*, Vol. 11, p. 10-24, 1991.

[52] S. C. Huang, M. E. Phelps, E. J. Hoffman, K. Sideris, C. J. Selin, and D. E. Kuhl, "Noninvasive determination of local cerebral metabolic rate of glucose in man," *Amer. Physiological Society*, E69-E82, 1980.

[53] L. A. Shepp and B. F. Logan, "The Fourier reconstruction of a head section," *IEEE Transactions on Nuclear Science*, NS-21, p. 21-43, June 1974.

[54] L. A. Shepp and Y. Vardi, "Maximum likelihood reconstruction for emission tomography," *IEEE Transactions on Medical Imaging*, MI-1, No. 2, p. 113-122, Oct. 1982.

[55] Z. H. Cho, Joie Jones, and Manbir Singh, *Foundations of Medical Imaging*, John Wiley & Sons, Inc., New York, 1993.

[56] L. G. Strauss and P. S. Conti, "The applications of PET in clinical oncology," *Journal of Nuclear Medicine*, Vol. 32, No. 4, p. 623-648, Apr. 1991.

[57] E. Tanaka and H. Murayama, "Properties of statistical noise in positron emission tomography," *Proc. Int. Workshop Phys. Eng. Med. Imaging*, New York: IEEE, p. 158-164, 1982.

[58] G. D. Tourassi and C. E. Floyd, "Artificial neural networks for single photon emission computed tomography: a study of cold lesion detection and location," *Investigative Radiology*, Vol 28, No. 8, p. 671-677, Aug. 1993.

[59] F. Turkheimer, R. M. Moresco, G. Lucignani, *et al.*, "The use of spectral analysis to determine regional cerebral glucose utilization with positron emission tomography and [^{18}F]fluorodeoxyglucose: theory, implementation, and optimization procedures," *Journal Cerebral Blood Flow and Metabolism*, 14:406-422, 1994.

[60] Let's Play PET, *http://www.crump.ucla.edu/lpp*

[61] Y. Vardi, L. A. Shepp, and L. Kaufman, "A statistical model for positron emission tomography," *Journal Ameri. Associ.*, Vol. 80, No. 389, 8-20, March 1985.

[62] M. Viberg and B. Ottersten, "Sensor array processing based on subspace fitting," *IEEE Transactions on Signal Processing*, Vol. 39, No. 5, p. 1110-1121, May 1991.

[63] R. L. Wahl, "Positron emission tomography: application in oncology" *Nuclear Medicine in Clinical Diagnosis and Treatment*, edited by I. P. C. Murray and P. J. Ell, Vol. 2, p. 801-820.

[64] R. L. Wahl, G. D. Hutchins, D. J. Buchsbaum, M. Liebert, H. B. Grossman, and S. Fisher, "18F-2-deoxy-2-fluoro-D-glucose uptake into human tumor xenografts. Feasibility studies for cancer imaging with positron-emission tomography," *Cancer*, Vol. 67, p. 1544-1550, 1991.

[65] R. L. Wahl, R. Cody, G. D. Hutchins, and E. Mudgett, "Primary and metastatic breast carcinoma: initial clinical evaluation with PET with the radiolabeled glucose analog 2-[F-18]-fluorodeoxy-2-D-glucose(FDG)," *Radiology*, Vol. 179, p. 765-770, 1991.

[66] D. W. Wilson and M. W. Benjamin, "Noise properties of filtered-backprojection and ML-EM reconstructed emission tomographic images," *IEEE Transactions on Nuclear Medicine*, Vol. 40, No. 4, p. 1198-1203, Aug. 1993.

[67] X. Yu, I. S. Reed, and A. Stocker, "Performance comparison of adaptive multi-band optical target detection," *IEEE Transactions on Signal Processing*, Aug. 1993.

[68] X. Yu, *et al.*, "A linear feature mapping framework for adaptive detection and recognition of targets in complex SAR data," *IEEE 28th Conference on Signal, System and Computers*, Monterey, CA, Oct. 30 - Nov. 2, 1994.

[69] X. Yu, J. R. Bading, and P. S. Conti, "Automated lesion detection with feature analysis in positron emission tomography," *IEEE Medical Imaging Conference*, Norfolk, Virginia, Nov. 3-6, 1994.

[70] X. Yu, A. M. Chen, and I. S. Reed, "A maximum likelihood detection of signals using feature mapping framework," *to appear in Proc. IEEE ICASSP,* Detroit, MI, May 1995.

[71] X. Yu and I. S. Reed "Adaptive detection of signals with feature linear mappings and representations," *IEEE Transactions on Signal Processing,* Vol. 43, No. 12, Dec. 1995.

[72] X. Yu, C. C. Huang, R. M. Leahy, J. R. Bading, and P. S. Conti, "Analytic computation and sample estimation of the local statistics of positron emission tomography images: a comparative study," *Proceedings of the 43rd Annual Meeting of the SNM,* Denver, Colorado, June 3-5, 1996.

[73] X. Yu and C. C. Huang, "Lesion detection with statistical model-based prior information in positron emission tomography," *IEEE Medical Imaging Conference,* Anaheim, CA, Nov. 2-9, 1996.

[74] X. Yu, L. E. Hoff, I. S. Reed,*et al.*, "Automated target detection and recognition in multiband imagery: a unified ML detection and estimation approach," *IEEE Transactions on Image Processing,* Vol. 6, No. 1, p. 134-156, Jan. 1997.

[75] X. Yu, C. C. Huang, J. R. Bading, and P. S. Conti, "Use of a matched subspace filter for lesion detection in dynamic positron emission tomography," submitted to *Annual Meeting of Soc. of Nuclear Medicine,* June 2-5, 1997, San Antonio, TX.

Appendix B: A Paper Presented in IEEE Medical Imaging Conference 1999

A New Method of Computer-Aided Feature Identification for Lesion Detection in PET-FDG Dynamic Study [1]

Chung-Chieh Huang[2] and Xiaoli Yu [3]
[2]Electrical Engineering Department, University of Southern California, CA 90089
[3]Radiology Department, University of Southern California, CA 90033

Abstract

Computer-aided feature identification in PET-FDG dynamic data is crucial to assist visual inspection for small lesion detection. It has been shown that the kinetic features of time activity curves (TAC) have the following properties: (a) linearly representable by a set of exponential functions, (b) physiologically distinguishable as lesion and normal tissue subspaces, (c) readily incorporable to a matched subspace detector for lesion detection. To identify the TAC subspace features, the least square error (LSE) method is often used to determine the lesion and normal tissue subspaces respectively. The subspaces resulted from the LSE are optimum in terms of the fidelity to the observed data, but they may suffer from a lack of the separability between subspaces. In this paper, a new method is proposed to maximize the distance (separability) between lesion and normal tissue subspaces under the constraint that the LSE (fidelity) of the estimated and observed TACs is less than a given value. Such identified subspaces are incorporated into a matched subspace detector for lesion detection. Results showed that the subspaces identified by the proposed method from known lesion and normal tissues mostly preserve the TAC kinetic features and increase the contrast of the small lesion to normal tissues compared to the LSE-only method.

I. Introduction

Positron emission tomography (PET)-scanning of $[^{18}]F$ fluorodeoxyglucose (FDG)-labeled tissues is becoming useful for the non-invasive diagnosis of cancer [1]. However, as with all nuclear medicine imaging technologies, lesion detection with PET-FDG is restricted by a relatively limited spatial resolution and a low signal-to-noise ratio, both rendering diagnosis by visual inspection difficult and potentially inaccurate, especially when the lesion diameter is less than 1 cm. Hence, computer-aided detection algorithms, e.g., feature identification, have been developed to assist visual inspection in PET tumor detection. The difficulty in computer-aided detection is that spatial features such as the shape or contrast of a lesion often vary from case-to-case and are hardly to identify.

It has been shown [4] that the kinetic features of time activity curves (TAC) from PET-FDG dynamic data have the following relatively *invariant* properties: (a) linearly representable by a set of exponential functions, (b) physiologically distinguishable as lesion and normal tissue subspaces, (c) readily incorporable to a matched subspace detector for lesion detection. To identify the TAC subspace features, the least square error (LSE) criterion is often used to estimate the lesion and normal tissue subspaces, respectively. The subspaces resulted from the LSE are optimum in terms of the fidelity to the observed data, but they may suffer from a lack of the separability between lesion and normal tissue when used for lesion detection. In order to enhance the lesion detection performance, we propose a new method for subspace identification which maximizes the separability (subspace angle [3]) between lesion and normal tissue subspaces and simultaneously preserves the fidelity of the estimated and observed TACs to a certain extent. A matched subspace detector utilizing the generalized likelihood ratio test [7] is applied to demonstrate the lesion detection improvement by the new subspace identification.

II. 4-k Compartmental Model Analysis

From a physiological compartment model analysis, a PET-FDG dynamic study can be interpreted as describing the passage of administered tracer through a finite number of independent homogeneous compartments [5, 6]. Each compartment is associated with a particular dynamic structure in the study and is described by a fundamental TAC (a physiological factor or a subspace basis). In this paper, the homogeneous model is assumed for the tissue region of interest (ROI) [8]. Fig.1 (a) shows a common 4-k compartment model for the FDG transfer in a homogeneous tissue: FDG in plasma ($C_p^*(t)$), FDG in tissue ($C_e^*(t)$), and phosphorylated FDG, FDG-6-P, in tissue ($C_m^*(t)$), where k_is are the tracer exchange rates between the compartments and $*$ indicates decay-corrected FDG quantities. The following equations describe the rate of change in the concentrations of FDG and FDG-6-P

$$\begin{aligned} \frac{dC_e^*(t)}{dt} &= K_1^* C_p^*(t) - (k_2^* + k_3^*) C_e^*(t) + k_4^* C_m^*(t), \\ \frac{dC_m^*(t)}{dt} &= k_3^* C_e^*(t) - k_4^* C_m^*(t). \end{aligned} \quad (1)$$

Given that the initial conditions $C_e^*(0) = C_m^*(0) = 0$, solutions of (1) show that the total tissue radioactivity, $C^*(t)$, is the sum of the free FDG concentration plus the concentration of metabolites, i.e.,

$$C^*(t) = C_e^*(t) + C_m^*(t) = [A_1 e^{-a_1 t} - A_2 e^{-a_2 t}] \otimes C_p^*(t), \quad (2)$$

[1]This work was supported in part by STOP CANCER Foundation and the U.S. Army Breast Cancer Research Project.

where

$$\alpha_{1,2} \triangleq \frac{1}{2}[(k_2^*+k_3^*+k_4^*) \mp \sqrt{(k_2^*+k_3^*+k_4^*)^2-4k_2^*k_4^*}],$$
$$A_1 \triangleq \frac{k_1^*}{\alpha_2-\alpha_1}(k_3^*+k_4^*-\alpha_1),$$
$$A_2 \triangleq \frac{k_1^*}{\alpha_2-\alpha_1}(\alpha_2-k_3^*-k_4^*), \quad (3)$$

and $\circledcirc$ denotes convolution. Under the homogeneous assumption, the PET-FDG time activity curve can be described as

$$\bar{C}_{\text{total}}^*(t) = V_a C_p^*(t) + (1-V_a)\cdot \bar{C}^*(t)$$
$$= V_a C_p^*(t) + [M_1 e^{-\alpha_1 t} - M_2 e^{-\alpha_2 t}] \circledcirc C_p^*(t), \quad (4)$$

where $M_1 \triangleq (1-V_a)A_1$ and $M_2 \triangleq (1-V_a)A_2$. The input plasma function, $C_p^*(t)$, in (4) is often measured. In this paper, $C_p^*(t)$ is modeled as a function given in [2]

$$C_p^*(t) = [B_1(t-\tau)-B_2-B_3]e^{-\lambda_1(t-\tau)} + B_2 e^{-\lambda_2(t-\tau)} + B_3 e^{-\lambda_3(t-\tau)}, \quad (5)$$

where λ_1, λ_2, and λ_3 are the eigenvalues of the blood circulatory system (1/min); B_1, B_2, and B_3 are the coefficients (μCi/ml); τ is the delay constant (min). A substitution of (5) into (4) yields the following expression for $\bar{C}_{\text{total}}^*(t)$,

$$\bar{C}_{\text{total}}^*(t) = E_1 t e^{-\lambda_1 t} + E_2 e^{-\lambda_1 t} + E_3 e^{-\lambda_2 t} + E_4 e^{-\lambda_3 t} + E_5 e^{-\alpha_1 t} + E_6 e^{-\alpha_2 t}, \quad (6)$$

where $\{E_1, E_2, E_3, E_4, E_5, E_6\}$ denote the coefficients of the corresponding exponential functions. In (6), the first four terms, denoted by the set $\mathcal{I} = \{te^{-\lambda_1 t}, e^{-\lambda_1 t}, e^{-\lambda_2 t}, e^{-\lambda_3 t}\}$, are contributed from the input plasma function and are common for all tissues, while the last two terms depend on the different tissue types and are denoted by the sets $\mathcal{L} \triangleq \{e^{-\alpha_1^{(l)} t}, e^{-\alpha_2^{(l)} t}\}$ and $\mathcal{B} \triangleq \{e^{-\alpha_1^{(b)} t}, e^{-\alpha_2^{(b)} t}\}$, where the superscripts (l) and (b) are for lesion and normal tissues, respectively.

III. Spatial-Temporal Date and Subspace Identification

Let P denote the number of pixels in an ROI and K be the frame number in a PET-FDG dynamic study, the observations of K TAC samples, $\bar{C}_{total}^*(t_i)$ in (6), in the p-th pixel of the ROI can be represented as

$$\mathbf{y}_p = [\bar{C}_{total}^*(t_1), \bar{C}_{total}^*(t_2), \cdots, \bar{C}_{total}^*(t_K)]^T + \mathbf{n}_p$$
$$= \mathbf{Q}\theta_p + \mathbf{n}_p, \quad (7)$$

where $\theta_p \triangleq [E_{1p}, E_{2p}, \cdots, E_{6p}]^T$ and $p = 1, 2, ..., P$. Each column of the matrix $\mathbf{Q}$ is composed of one exponential function in (6) sampled at $t_1, \cdots, t_K$. For a TAC in a lesion, $\mathbf{Q} = [\mathbf{I}, \mathbf{L}]$, while for a TAC in normal tissues, $\mathbf{Q} = [\mathbf{I}, \mathbf{B}]$. The notations $\mathbf{I}$, $\mathbf{L}$, and $\mathbf{B}$ are vector representations of the sets $\mathcal{I}$, $\mathcal{L}$, and $\mathcal{B}$, respectively. In (7), $\mathbf{n}_p$ denotes the noise and is assumed to be white Gaussian. Then, the PET-FDG dynamic data can be formed into a spatial-temporal matrix

$$\mathbf{M}_{K\times P} \triangleq [\mathbf{y}_1, \mathbf{y}_2, \cdots, \mathbf{y}_P] = \mathbf{QA} + \mathbf{N}, \quad (8)$$

where $\mathbf{A} \triangleq [\theta_1, \theta_2, \cdots, \theta_P]$ and $\mathbf{N} \triangleq [\mathbf{n}_1, \mathbf{n}_2, \cdots, \mathbf{n}_P]$. The matrix $\mathbf{Q}$ is unknown and often estimated from the spatial-temporal data matrix $\mathbf{M}$ using the least square error (LSE) criterion. If the data matrix $\mathbf{M}$ contains a known tumor (or normal tissue), the column vectors of $\hat{\mathbf{Q}}$, the estimate of $\mathbf{Q}$, span a lesion (or normal tissue) subspace. Thus the estimation of unknown parameters of $\mathbf{Q}$ is also called the subspace identification. In this paper, the unknown parameters of exponential vectors in $\mathbf{Q}$ are estimated by the Newton-Raphson algorithm [6] from data $\mathbf{M}$, which achieves the least square error.

IV. Subspace Refining for Lesion Detection

The lesion and normal tissue subspaces estimated individually by the least square error (LSE) method from the known types of tissue data generally capture the most characteristics of lesion and normal tissues, respectively. But the two resulting subspaces may be so close to each other that hardly to be separated. The subspace refining post to the subspace identification is to select two subsets of basis vectors (column vectors) from the identified subspaces $\mathbf{Q}^{(l)} = [\mathbf{I}, \hat{\mathbf{L}}]$ and $\mathbf{Q}^{(b)} = [\mathbf{I}, \mathbf{B}]$ based on the subspace distance maximization (separability) between the two candidate subsets, subject to the condition that the LSEs (fidelities) are less than given values. The sets, $\hat{\mathbf{L}}$ and $\hat{\mathbf{B}}$, must be included in the selected subsets for lesion and normal tissues, respectively, because they characterize different tissue types in (2). Thus, the problem is simplified to choose basis vectors from the input plasma vector set $\hat{\mathbf{I}}$ which is common for all tissue types. Usually, three basis vectors are enough to represent the TAC subspace features [4], therefore, only one basis vector is needed from $\hat{\mathbf{I}}$ to form the lesion subspace $\mathbf{H}$ and normal tissue subspace $\mathbf{S}$, respectively. The new criterion is described as follows: given $\mathbf{H}' = \hat{\mathbf{L}} \cup \{\mathbf{h}\}$ and $\mathbf{S}' = \hat{\mathbf{B}} \cup \{\mathbf{s}\}$, where the vectors $\mathbf{h}, \mathbf{s} \in \hat{\mathbf{I}}$,

$$\mathbf{H}, \mathbf{S} = \arg\max_{\mathbf{H}', \mathbf{S}'} distance\{\mathbf{H}', \mathbf{S}'\}, \text{ subject to}$$
$$||\mathbf{M} - \mathbf{P}_{H'}\mathbf{M}||_F < \epsilon_1 \text{ and } ||\mathbf{M} - \mathbf{P}_{S'}\mathbf{M}||_F < \epsilon_2, \quad (9)$$

where $distance\{\mathbf{H}, \mathbf{S}\}$ is the subspace distance defined as $distance\{\mathbf{H}, \mathbf{S}\} = \sqrt{1-r_1^2}$, ($r_1$ is the largest principal correlation coefficient between $\mathbf{H}$ and $\mathbf{S}$, [3]), $\mathbf{M}$ is the PET-FDG dynamic data in (8), $\mathbf{P}_H$ is the orthogonal projection matrix onto the subspace of $\mathbf{H}$, $||\cdot||_F$ denotes the Frobenius norm, and ϵ_1 and ϵ_2 are the thresholds set for the least square error.

V. Matched Subspace Detection

From the K-dimensional data $\mathbf{y}$, we must decide between *two* possible hypotheses regarding how the data was generated [7]. Based on a replacement model, the null hypothesis H_0 says

that the data consists of a sum of normal tissue signal $\mathbf{x}_0$ and noise $\mathbf{n}_0$; the alternate hypothesis H_1 says that the data consist of a sum of lesion signal $\mathbf{x}_1$ and noise $\mathbf{n}_1$. That is

$$H_0 : \mathbf{y} = \mathbf{x}_0 + \mathbf{n}_0 \quad \text{and} \quad H_1 : \mathbf{y} = \mathbf{x}_1 + \mathbf{n}_1. \tag{10}$$

The noise $\mathbf{n}_i$ is assumed to be normal with zero mean and covariance matrix $\sigma_i^2\mathbf{I}$, and the signal $\mathbf{x}_i$ is assumed to obey the linear subspace model

$$\begin{aligned} \mathbf{x}_0 &= \mathbf{S}\boldsymbol{\phi}, \ \mathbf{S} \in \mathcal{R}^{K\times t}, \ \boldsymbol{\phi} \in \mathcal{R}^t, \ t < K - p, \\ \mathbf{x}_1 &= \mathbf{H}\boldsymbol{\theta}, \ \mathbf{H} \in \mathcal{R}^{K\times p}, \ \boldsymbol{\theta} \in \mathcal{R}^p, \end{aligned} \tag{11}$$

where $\mathbf{H}\boldsymbol{\theta}$ is a lesion-bearing signal that lies in the lesion subspace $\langle\mathbf{H}\rangle$, $\mathbf{S}\boldsymbol{\phi}$ is a normal tissue signal that lies in the normal tissue subspace $\langle\mathbf{S}\rangle$, and $\boldsymbol{\theta}$ and $\boldsymbol{\phi}$ are the corresponding coefficients. The columns of $\mathbf{H}$ and $\mathbf{S}$ are the basis for the subspaces $\langle\mathbf{H}\rangle$ and $\langle\mathbf{S}\rangle$, respectively. The subspaces $\langle\mathbf{H}\rangle$ and $\langle\mathbf{S}\rangle$ are not orthogonal, but they are linearly independent. Then the detection problem becomes a test of the distributions

$$H_0 : \mathbf{y} : N[\mathbf{S}\boldsymbol{\phi}, \sigma_0^2\mathbf{I}] \quad \text{and} \quad H_1 : \mathbf{y} : N[\mathbf{H}\boldsymbol{\theta}, \sigma_1^2\mathbf{I}]. \tag{12}$$

The likelihood ratio test can be written as

$$\begin{aligned} l(\mathbf{y}) &= \frac{l(\boldsymbol{\theta}, \sigma_1^2; \mathbf{y})}{l(\boldsymbol{\phi}, \sigma_0^2; \mathbf{y})} \\ &= \left(\frac{\sigma_1^2}{\sigma_0^2}\right)^{-K/2} \exp\left\{-\frac{1}{2\sigma_1^2}||\mathbf{n}_1||_2^2 + \frac{1}{2\sigma_0^2}||\mathbf{n}_0||_2^2\right\}. \end{aligned} \tag{13}$$

Hence, the *generalized likelihood ratio test* (GLRT) can be derived by substituting the maximum likelihood estimate (MLE), $\hat{\sigma}_i$ and $\hat{\mathbf{n}}_i$, of σ_i and $\mathbf{n}_i$, respectively,

$$\hat{l}(\mathbf{y}) = \left(\frac{\hat{\sigma}_1^2}{\hat{\sigma}_0^2}\right)^{-K/2} \exp\left\{-\frac{1}{2\hat{\sigma}_1^2}||\hat{\mathbf{n}}_1||_2^2 + \frac{1}{2\hat{\sigma}_0^2}||\hat{\mathbf{n}}_0||_2^2\right\}, \tag{14}$$

where $\hat{\mathbf{n}}_0 = \mathbf{P}_S^{\perp}\mathbf{y}$, $\hat{\mathbf{n}}_1 = \mathbf{P}_H^{\perp}\mathbf{y}$, and $\hat{\sigma}_i^2 = \frac{1}{K}||\hat{\mathbf{n}}_i||_2^2$. It is more convenient to replace the GLRT by the $(K/2)$-root GLRT. hence, the GLRT for the replacement hypothesis model becomes

$$L_R(\mathbf{y}) = [\hat{l}(\mathbf{y})]^{2/K} = \frac{||\hat{\mathbf{n}}_0||_2^2}{||\hat{\mathbf{n}}_1||_2^2} = \frac{\mathbf{y}^T\mathbf{P}_S^{\perp}\mathbf{y}}{\mathbf{y}^T\mathbf{P}_H^{\perp}\mathbf{y}}. \tag{15}$$

VI. Experiment and Result

Two PET-FDG dynamic studies, one lung cancer and one breast cancer, acquired with the USC ECAT953 scanner, were used in this paper. Fig.2 (a) showed the lung cancer FBP image in the dynamic data, where two 5×5 ROIs were selected from one known lesion (L1) and one normal tissue (BG), and their corresponding TACs were plotted in Fig.2 (b). Also one plasma ROI was drawn from the heart area for the plasma parameter estimation. The L1, BG, and plasma ROI data were used to estimate the parameters in (6) by the Newton-Raphson method [6] to form the matrix $\mathbf{L}$, $\mathbf{B}$, and $\mathbf{I}$, from which two sets of basis vectors were selected to form the subspaces for lesion ($\mathbf{H}$) and normal tissue ($\mathbf{S}$) by using the new criterion in (9). The fidelity between the estimated TAC by the identified subspaces and the observed TAC was shown in Fig.2 (c-d). The separability was demonstrated in Fig.2 (e) by projecting the L2 TAC (shown in Fig.1 (a)) onto the identified lesion and normal tissue subspaces, respectively. The refined subspaces by the new criterion were applied to the matched subspace detector in (15). The GLRT was performed on the test region indicated by a rectangle in Fig.2 (f). The result was shown in Fig.2 (h). It was demonstrated that the contrast of the small lesion (L2) to the normal tissues was improved compared to the previous detection result [4] shown in Fig.2 (g) which was obtained by the LSE-only criterion. Fig.3 (a-f) showed the results for the breast cancer study by applying the proposed method. The comparison of the lesion-to-background contrast enhancement was shown in Table 1.

VII. Conclusion

In lesion detection with PET-FDG dynamic studies, kinetic features (subspaces) of the time activity curves (TAC) are usually estimated by the least square error (LSE) method. In this paper, a new method was demonstrated to maximize the distance (separability) between lesion and normal tissue subspaces under the constraint that the LSEs (fidelity) of the estimated and observed TACs are less than given values. Such identified and refined subspaces are incorporated into a matched subspace detector for lesion detection. Results showed that the subspaces obtained by the proposed method from known lesion and normal tissues mostly preserve the TAC kinetic features and increase the separability of the small lesion from normal tissues compared to the LSE-only method.

VIII. References

[1] P. S. Conti *et al.*, "PET and [^{18}F]-FDG in oncology: a clinical update," *Nuclear Medicine and Bio.*, Vol: 23, p. 717-735, 1996.

[2] D. Feng and X. Wang, "A computer simulation study on the effects of input function measurement noise in tracer kinetic modeling with positron emission tomography (PET)," *Comput. Bio. Med.*, Vol. 23, No. 1, p. 57-68, 1984.

[3] G. H. Golub and C. F. Van Loan, *Matrix Computations,* Johns Hopkins, 3rd edition, 1996.

[4] C. C. Huang, X. Yu, J. Bading, and P. S. Conti, "Feature extraction by subspace fitting of time activity curve in PET dynamic studies," *IEEE Medical Image Conference,* Nov. 1997.

[5] S. C. Huang, M. E. Phelps, E. J. Hoffman, K. Sideris, C. J. Selin, and D. E. Kuhl, "Noninvasive determination of local cerebral metabolic rate of glucose in man," *Amer. Physiological Society,* E69-E82, 1980.

[6] M. E. Phelps, J. C. Mazziotta, and H. R. Schelbert, *Positron Emission Tomography and Autoradiology, Principles and Applications for the Brain and Heart,* Raven Press, 1986.

[7] L. L. Scharf and B. Friedlander, "Matched subspace detectors," *IEEE Trans. on Signal Processing,* Vol. 42, No. 8, p. 2146-2157, Aug. 1994.

[8] K. Schmidt, G. Mies, and L. Sokoloff, "Model of kinetic behavior of deoxyglucose in heterogeneous tissues in brain: A reinterpretation of the significant of parameters fitted to homogeneous tissue models," *J. Cerebral Blood Flow and Metabolism,* Vol. 11, p. 10-24, 1991.

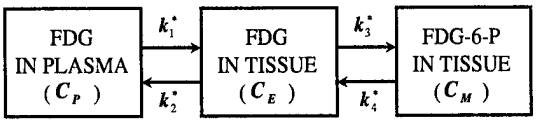

Fig. 1 A 4-k compartment model.

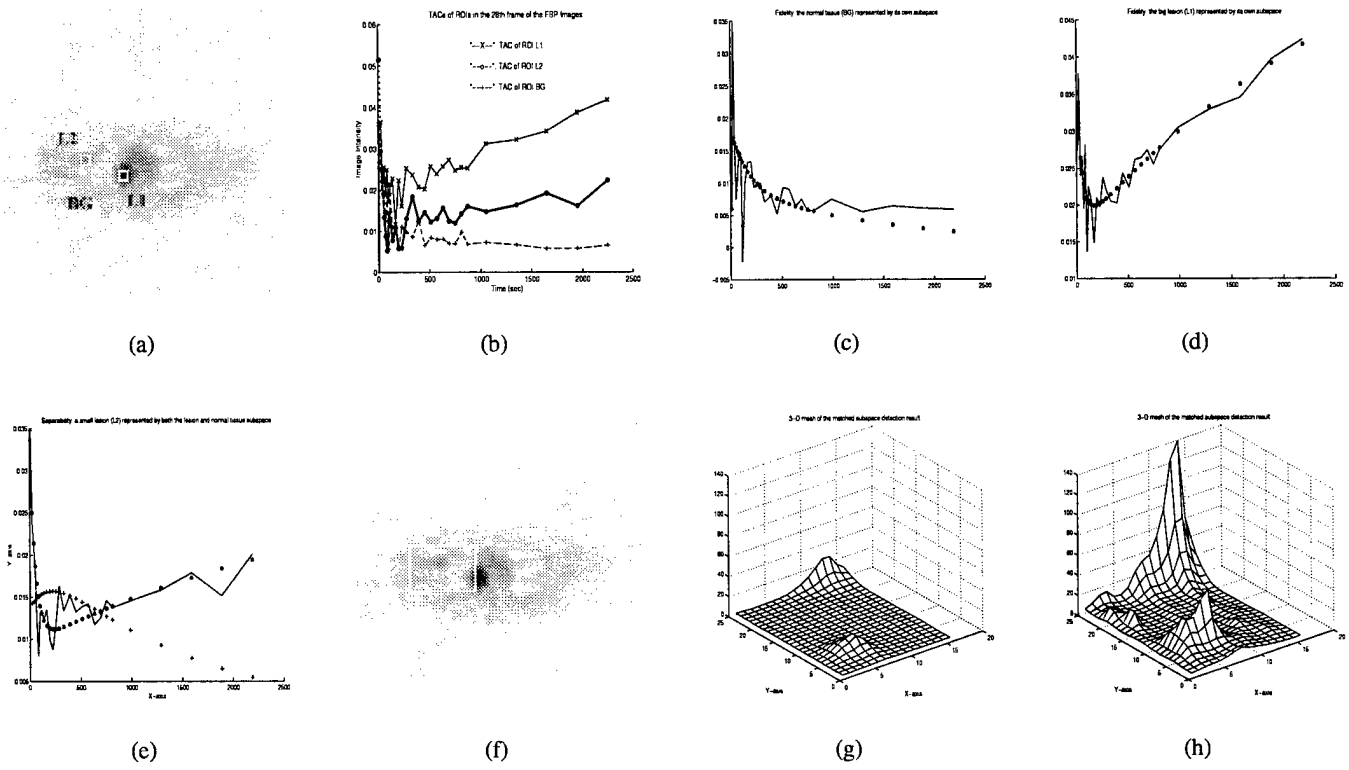

Fig. 2 **Lung cancer study** (a): A PET-FDG dynamic lung cancer image with three ROIs selected: L1 (big lesion), L2 (small lesion), and BG (normal tissue). (b): TACs for L1 (upper), L2 (middle), and BG (lower). (c-d): Fidelity test: the L1 and BG TACs represented by their own estimated subspaces. (e): Separability test: the L2 TAC represented by the estimated lesion and normal tissue subspaces. (f): A test region indicated by a rectangle. 3-D mesh of the GLRT detection result by (g): the LSE-only method, and (h): the proposed method.

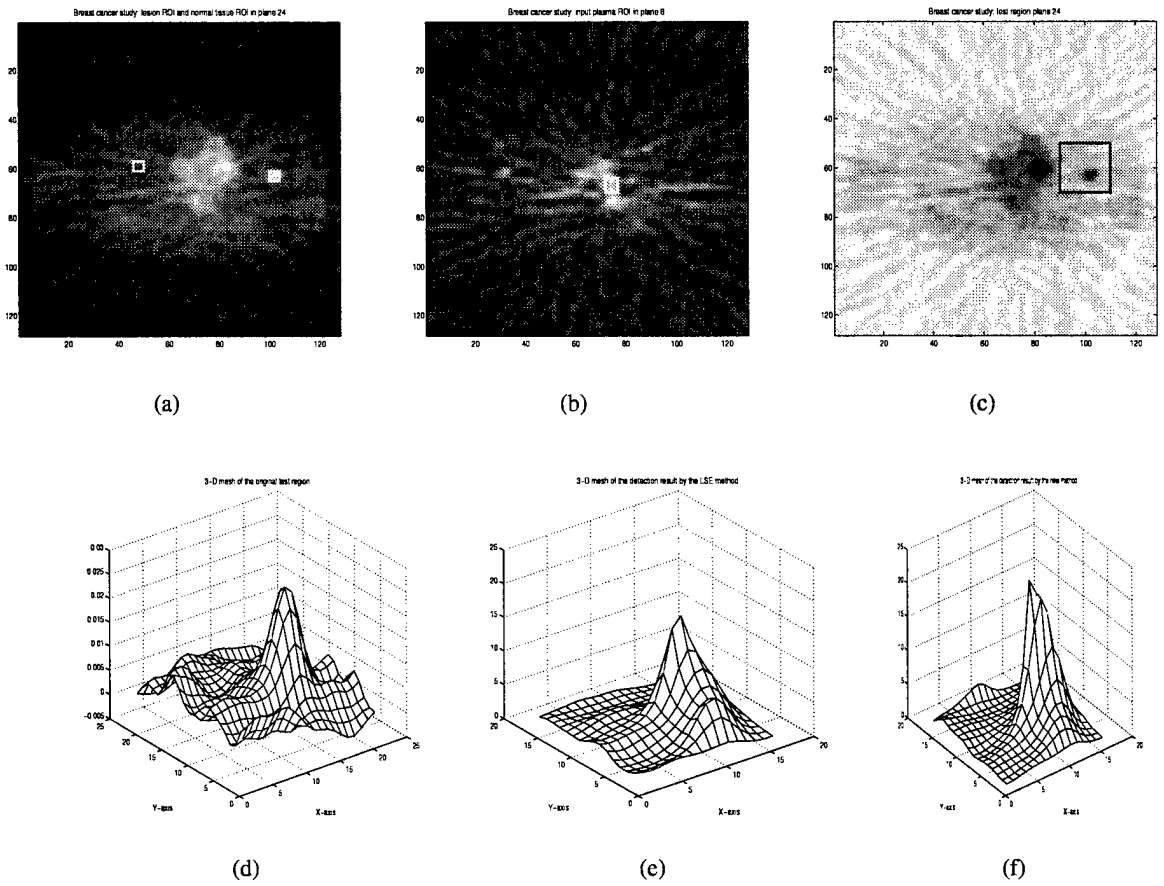

Fig. 3 **Breast cancer study** (a): A PET-FDG dynamic breast cancer data with two ROIs selected: lesion (right) and normal tissue (left). (b): Input plasma ROI. (c): A test region indicated by a rectangle. (d): 3-D mesh of the test region. 3-D mesh of the GLRT detection result by (e): the LSE-only method, and (f): the proposed method.

Table 1: Lesion-to-Background Contrast Enhancement

$$\text{Lesion-to-background contrast} \triangleq \frac{\text{peak value in lesion ROI}}{\text{mean value of background}}$$

Dynamic Study	Contrast in Original Image (a)	Contrast in GLRT by the LSE-Only Method (b)	Contrast in GLRT by the New Method (c)	Contrast Enhancement (c) to (a)	Contrast Enhancement (c) to (b)
Lung Cancer (small lesion: L2)	4.29	4.32	4.55	6%	5%
Breast Cancer	5.7	7.3	12.9	126%	77%

Appendix C: Manuscript revised for submission to IEEE Trans. on Medical Image Processing

Data Reduction for Fast Dynamic PET Reconstruction and SNR Enhancement *

Piyapong Thanyasrisung[1], Xiaoli Yu[1,2] and Chungchi Huang
[1]Department of Electrical Engineering
[2]Department of Radiology
University of Southern California, Los Angeles, CA 90089

August 30, 2000

Abstract

The reconstruction of dynamic positron emission tomograph (PET) images is time consuming. Previous work to speed up the dynamic image reconstruction was based on low-order approximation using Karhunen-Loève (KL) transform. Those KL transform basis vectors corresponding to the largest K eigenvalues were retained and then used in the reconstruction process. However, with this approach the kinetic characteristic (time activity curves) of week signals, such as non-palpable tumors, may be lost or significantly changed in the reconstructed images. In this paper, a metric is found to select a subset of vectors from the KL transform basis, which relates directly to maximizing lesion-to-background ratio (signal-to-noise ratio). The results using computer simulation PET data show that by this approach the contrast of small lesion to the background can be objectively enhanced. The characteristic of time activity curve in the lesions can also be approximately kept.

1 Introduction

In a dynamic positron emission tomographic (PET) study, multiple frames of *sinogram* are acquired and formed into a multi-frame raw data matrix. Each frame is observed at a different time. In the conventional dynamic PET image reconstruction, each frame of data matrix is reconstructed separately by the filtered backprojection (FBP), which is an approximation of the inverse Radon transform. From these frames of reconstructed images, a diagnosis of the abnormal tissue (or malignant lesions) can be made by examining the differences in kinetics of the time activity curve between the normal and abnormal tissue [5].

The conventional dynamic image reconstruction is highly time consuming. Also the reconstructed images are often noisy. Recent efforts have been made to suppress noise level in the sinogram, while lowering the computation complexity by the reduction of data dimensionality in time domain. Research in [4], [6] shows that by compressing the data with the sample-estimated Karhunen-Loève (KL) transform along the time axis of the sinogram data, one can speed up the reconstruction procedure and also suppress the noise. In this approach one keeps only K dominant eigenvalues of the sample-estimated covariance matrix in time and the corresponding eigenvectors. In this manner, the amount of compressed data tends to minimize the distortion from the original data. For example, if the number of frame is 28, then keeping only $K = 5$ of the eigenvectors in the KL transformation can basically secure the fidelity of the main structures in the reconstructed images. Thus the image reconstruction can be significantly speeded up by reconstructing 5 frames of the KL transformed sinogram, instead of 28 frames.

However, by keeping the K eigenvectors which have the dominant eigenvalues in the KL transform, weak structures of lesions may be lost in the reconstructed images, because such weak signals may not be of sufficient strength in these K kept dominant components. In the application of dynamic PET imaging

*This work is partially supported under the U.S. Army BCRP Idea Award.

to oncology, what desired is a rank-reduction algorithm that can keep the energy of weak lesions in the dimension-reduced data while suppressing the noise. It is also important that rank-reduction processing is able to retain the same difference of time activity curve between the normal and abnormal tissue as it would be without the rank reduction.

2 PROPOSED METHOD

To accomplish such a desired rank-reduction, let's first describe the data model to be used. It is well-known that PET raw sinogram can be approximated by the following discrete-imaging model,

$$E\{\underline{y}_k\} = \mathbf{h}\underline{\mu}_k, \quad k = 1, 2, \ldots, L \tag{1}$$

where L is the total number of frames in a dynamic acquisition, $\underline{y}_k$ is an $M \times 1$ vector obtained by a lexicographic ordering of the sinogram data matrix at frame k, $\underline{\mu}_k$ is an $N \times 1$ vector obtained by lexicographically ordering the original image data matrix at frame k and $\mathbf{h}$ is the $M \times N$ system matrix which represents the forward-projection process (i.e. the discrete Radon transform). The sinogram data $\{\underline{y}_k\}_{k=1}^{L}$ are collected by a PET scanner. The filtered backprojection of the sinogram data is utilized to estimate or reconstruct the images $\{\underline{\mu}_k\}_{k=1}^{L}$.

In our newly proposed method, the sample-estimated covariance matrix is first computed along the time axis of the data. Then K of L coefficients and the corresponding eigenvectors are selected by the maximum SNR per basis vectors criterion. Such selected K frames of KL transformed sinogram are reconstructed as K frames of KL transformed images. Then an inverse KL transform is performed on these K frames of the transformed image to obtain L frames of the original images. To see this, write eq.(1) in the following vector form,

$$E\{\mathbf{y}\} = \mathbf{H}\mu, \tag{2}$$

where

$$\begin{aligned} \mu &= [\underline{\mu}_1^\top \ \underline{\mu}_2^\top \ \cdots \ \underline{\mu}_L^\top]^\top, \\ \mathbf{y} &= [\underline{y}_1^\top \ \underline{y}_2^\top \ \cdots \ \underline{y}_L^\top]^\top \end{aligned} \tag{3}$$

are $LN \times 1$ and $LM \times 1$ vectors, respectively, and

$$\mathbf{H} = \begin{bmatrix} \mathbf{h} & & \mathbf{0} \\ & \mathbf{h} & \\ & & \ddots \\ \mathbf{0} & & \mathbf{h} \end{bmatrix} \tag{4}$$

is the $LM \times LN$ matrix which represents the operator of an L-frame forward projection or discrete Radon transform.

Also let $\tilde{\mathbf{y}}$ denote the KL-transform of the sinogram data vector $\mathbf{y}$, i.e.,

$$\tilde{\mathbf{y}} = \mathbf{A}\mathbf{y}, \tag{5}$$

and

$$\mathbf{A} = \mathbf{\Phi}^\top \otimes \mathbf{I}_M, \tag{6}$$

where $\mathbf{I}_M$ denotes the $M \times M$ identity matrix, and $\otimes$ denotes the Kronecker product. Next let $\mathbf{\Phi}$, the KL transformation matrix, be defined by the equation,

$$\mathbf{C}^{time} = \mathbf{\Phi}\mathbf{\Lambda}\mathbf{\Phi}^\top. \tag{7}$$

Here $\mathbf{C}^{time}$ is the temporal covariance matrix of the PET sinogram sequence and $\mathbf{\Lambda} = \mathrm{diag}(\lambda_1, \ldots, \lambda_L)$ is a matrix of the eigenvalues of $\mathbf{C}^{time}$. Without loss of generality, it can be assumed that the entries, λ_1, λ_2, ..., λ_L, of the diagonal matrix $\mathbf{\Lambda}$, are in a descending order. In the approach in [4], [6], the K

eigenvectors, denoted by $\phi_1,\ \phi_2,\ ...,\ \phi_K$, which correspond to the first K eigenvalues $\lambda_1,\ \lambda_2,\ ...,\ \lambda_K$, are chosen to perform a rank-reduced KL transformation given by

$$\hat{\tilde{\mathbf{y}}}_{SVD} = \hat{\mathbf{A}}_{SVD}\mathbf{y}, \tag{8}$$

where

$$\hat{\mathbf{A}}_{SVD} = \mathbf{\Phi}_{SVD}^{\top} \otimes \mathbf{I}_M \tag{9}$$

with the matrix $\mathbf{\Phi}_{SVD}$ defined by

$$\mathbf{\Phi}_{SVD} = [\phi_1,\ \phi_2,\ ...,\ \phi_K]. \tag{10}$$

In our approach, the criterion of the maximum signal-to-noise ratio (SNR) per basis vector is to simultaneously reduce the rank (or dimension) of the sinogram data in time domain and to enhance the signatures of weak lesion signals. To compute the SNR one needs prior knowledge of the lesion's kinetic signature. There are various methods to estimate the lesion kinetics either directly from raw dynamic sinogram sequence or from reconstructed image sequence [8][7]. In this paper, one assumes that the kinetics of lesion is known and denoted by $\mathbf{s}$. With knowledge of the lesion kinetic signature, taking the K maximum terms in the summation, which is known as the expression of (lesion) signal-to-noise ratio ,

$$\begin{aligned} \mathbf{s}^{\top}(\mathbf{C}^{time})^{-1}\mathbf{s} &= \mathbf{s}^{\top}(\Phi\Lambda^{-1}\Phi^{\top})\mathbf{s} \\ &= \sum_{k=1}^{L} \frac{|\mathbf{s}^{\top}\phi_k|^2}{\lambda_k} \end{aligned} \tag{11}$$

yields the desired subset of basis functions for the rank-reduction. This metric, in other words, is to choose K from L eigenvectors, resulting K maximal $\frac{|\underline{s}^{\top}\phi_k|^2}{\lambda_k}$, among $k = 1, 2, ..., L$. Let the selected K eigenvectors be the column vectors of matrix $\mathbf{\Phi}_{SNR}$, then the rank-reduced sinogram by the criterion of the maximum signal-to-noise ratios (SNR) per basis vector is

$$\hat{\tilde{\mathbf{y}}}_{SNR} = \hat{\mathbf{A}}_{SNR}\mathbf{y}, \tag{12}$$

where

$$\hat{\mathbf{A}}_{SNR} = \mathbf{\Phi}_{SNR}^{\top} \otimes \mathbf{I}_M. \tag{13}$$

Besides the maximum SNR per basis vector criterion, the other criterion studied in this paper for the purpose of comparison is the maximum signal energy per basis vector. Differing from the criteria of maximum eigenvalues and the maximum SNR per basis vector, the objective function of the maximum signal energy per basis vector is to select K out of L eigenvectors which maximize the variable $|\underline{s}^{\top}\phi_k|^2$, for $k = 1, 2, ..., L$, in the expression of lesion signal energy

$$\begin{aligned} \mathbf{s}^{\top}\mathbf{s} &= \mathbf{s}^{\top}(\Phi\Phi^{\top})\mathbf{s} \\ &= \sum_{k=1}^{L} |\mathbf{s}^{\top}\phi_k|^2. \end{aligned} \tag{14}$$

Let $\mathbf{\Phi}_{MSE}$ denote the matrix formed by the K eigenvectors selected in this manner. Then one has

$$\hat{\tilde{\mathbf{y}}}_{MSE} = \hat{\mathbf{A}}_{MSE}\mathbf{y}, \tag{15}$$

where

$$\hat{\mathbf{A}}_{MSE} = \mathbf{\Phi}_{MSE}^{\top} \otimes \mathbf{I}_M. \tag{16}$$

3 Simulation Results

A computer-simulated 28-frame dynamic phantom was used to demonstrate the performance of the rank-reduction algorithms. The simulated phantom consisted of five circular regions, see Fig. 1 for the phantom image. The smallest circle represents a lesion, the sencond smallest corresponds a heart, and the rest circles

represent the other parts of a chest image. The time activities in lesion, heart and normal tissues, which are obtained from a clinical PET scan and shown in Fig. 2, are assigned to the "tissues" in these circles, respectively. The "tissues" in the three larger circular regions in the images share the same time activity curve.

Three rank-reduction algorithms were applied to the simulated phantom in order to compare their performance. All three algorithms started with computing the sample-estimated covariance matrix of the sinogram data along time axis. Three different metrics were used to select $K = 5$ out of 28 eigenvalues and the corresponding eigenvectors. The first algorithm uses the maximum eigenvalue metric (also denoted as SVD method in this paper) , which keeps the K eigenvectors corresponding to the largest eigenvalues. The second employs the maximum signal-energy metric, and the third is the proposed algorithm which yields the maximum SNR per basis vector.

The steps of the simulation are summarized as follows.

Step 1: Generating 28 frames of sinogram data by the forward projection of the 28-frame phantom image sequence;

Step 2: Computing the sample-covariance matrix of the sinogram data along time axis;

Step 3: Applying the following 3 different metrics to reduce the rank (dimension) of the sinogram data in time domain

- Maximum eigenvalue (SVD)
- Maximum signal (lesion) energy (MSE)
- Maximum signal to noise ratio (SNR) per basis vector

Step 4: Selecting $K = 5$ from $L = 28$ eigenvectors according to the above three different criteria and forming the rank-reduced KL transformation matrices Φ_{SVD}, Φ_{MSE}, Φ_{SNR}, respectively;

Step 5: Reducing the rank of the sinogram $\mathbf{y}$ by applying the transformation $\hat{\mathbf{A}}_{(\cdot)} = \mathbf{\Phi}_{(\cdot)}^{\top} \otimes \mathbf{I}_M$ to the sinogram $\mathbf{y}$. The resulting rank-reduced sinogram denoted by $\hat{\tilde{\mathbf{y}}}_{(\cdot)}$ is given by

$$\hat{\tilde{\mathbf{y}}}_{(\cdot)} = \hat{\mathbf{A}}_{(\cdot)}\mathbf{y} \tag{17}$$

where the subscription $(\cdot)$ represents three different criteria: the SVD, MSE or SNR;

Step 6: Reconstructing the rank-reduced images from the rank-reduced sinogram $\hat{\tilde{\mathbf{y}}}_{(\cdot)}$ by the FBP;

Step 7: Expanding the rank-reduced images into a full rank by taking the corresponding inverse KL transformations.

The simulation results are shown in Fig, 3. From the reconstructed images of the 1^{st} frame, shown in Fig. 3 (b) - (d), the maximum SNR per basis vector criterion provides the best performance. The weak lesion (the smallest circular region), which is invisible in the FBP image reconstructed from the original sinogram without rank-reduction, becomes visible in the 1^{st} frame image obtained by the maximum SNR criterion. At the 28^{th} frame, lesion to background contrast in Fig. 3 (j) was reduced by the conventional SVD method compared to the original FBP reconstruction shown in Fig. 3 (i).

Fig. 3 (m) - (p) present the time activity curves of the lesion measured in the images reconstructed from the original sinogram and the sinograms processed with the maximum eigenvalue (SVD) criterion, the maximum signal (lesion) energy (MSE) criterion and the maximum SNR criterion, respectively. In both the SVD and MSE methods the time activity curves in the lesion were significantly changed.

4 CONCLUSION

In this paper, three rank-reduction criteria were applied to lower the dimensionality of dynamic sinogram in time domain. The simulation results show that by compressing the sinogram data before image reconstruction, one can speed up the reconstruction of dynamic images and also suppress the noise. The proposed

maximum SNR criterion outperforms the conventional SVD and the maximum signal energy methods in terms of enhancing lesion to background contrast in the reconstructed images. From the measured time activity curves in the images reconstructed from the sinograms processed with the three different rank reduction criteria, one can see that the maximum SNR method maintains the characteristics of the lesion time activity curve, while both the SVD and the maximum signal energy methods change the characteristics of time activity curve in the lesion substantially.

References

[1] J. S. Goldstein and I. S. Reed, "Reduced-Rank Adaptive Filtering," *IEEE Trans. Signal Processing,* Feb. 1997.

[2] J. S. Goldstein and I. S. Reed, "Theory of Partially Adaptive Radar," *IEEE Trans. Aerosp. Electron. Syst.,* Oct. 1997.

[3] F. Pedersen, M. Bergstrom, E. Bengtsson and B. Langstrom, "Principal component analysis of dynamic positron emission tomography images," *European Journal of Nuclear Medicine,* Vol. 21, No. 12, pp1285-1292, Dec. 1994.

[4] M. N. Wernick, E. J. Infusino and C. M. Kao, "Fast optimal pre-reconstruction filters for dynamic PET," *IEEE MIC Conference,* 1997.

[5] Simon R. Cherry and Michael E. Phelp, "Imaging brain function with positron emission tomography," in Arthur W. Toga and John C. Mazziotta, editors, *Brain Mapping: The Methods,* Chapter 8. Academic Press, 1996.

[6] C. M. Kao, J. T. Yap, J. Mukherjee and M. N. Wernick, "Image Reconstruction for Dynamic PET Based on Low-Order Approximation and Restoration of the Sinogram," *IEEE Trans. Medical Imaging,* Vol. 16, No. 6, Dec. 1997.

[7] C. C. Huang, X. Yu, J. Bading and P. S. Conti, "Feature extraction by subspace fitting of time activity curves in PET dynamic studies", *IEEE Medical Imaging Conference,* November 1997.

[8] R.H. Huesman, B. W. Reutter, G. L. Zeng, and G. T. Gullberg, "Kinetic parameter estimation from SPECT cone-beam projection measurements", *Phys Med Biol,* 43(4):973-982, 1998.

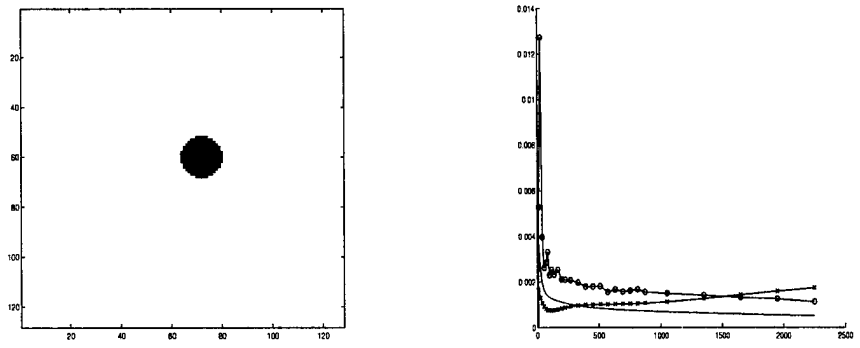

(a) (b)

Figure 1: (a) The phantom image. (b) Clinical TACs used for dynamic phantom simulation: '-' for normal tissue, 'x' for lesion, and 'o' for heart.

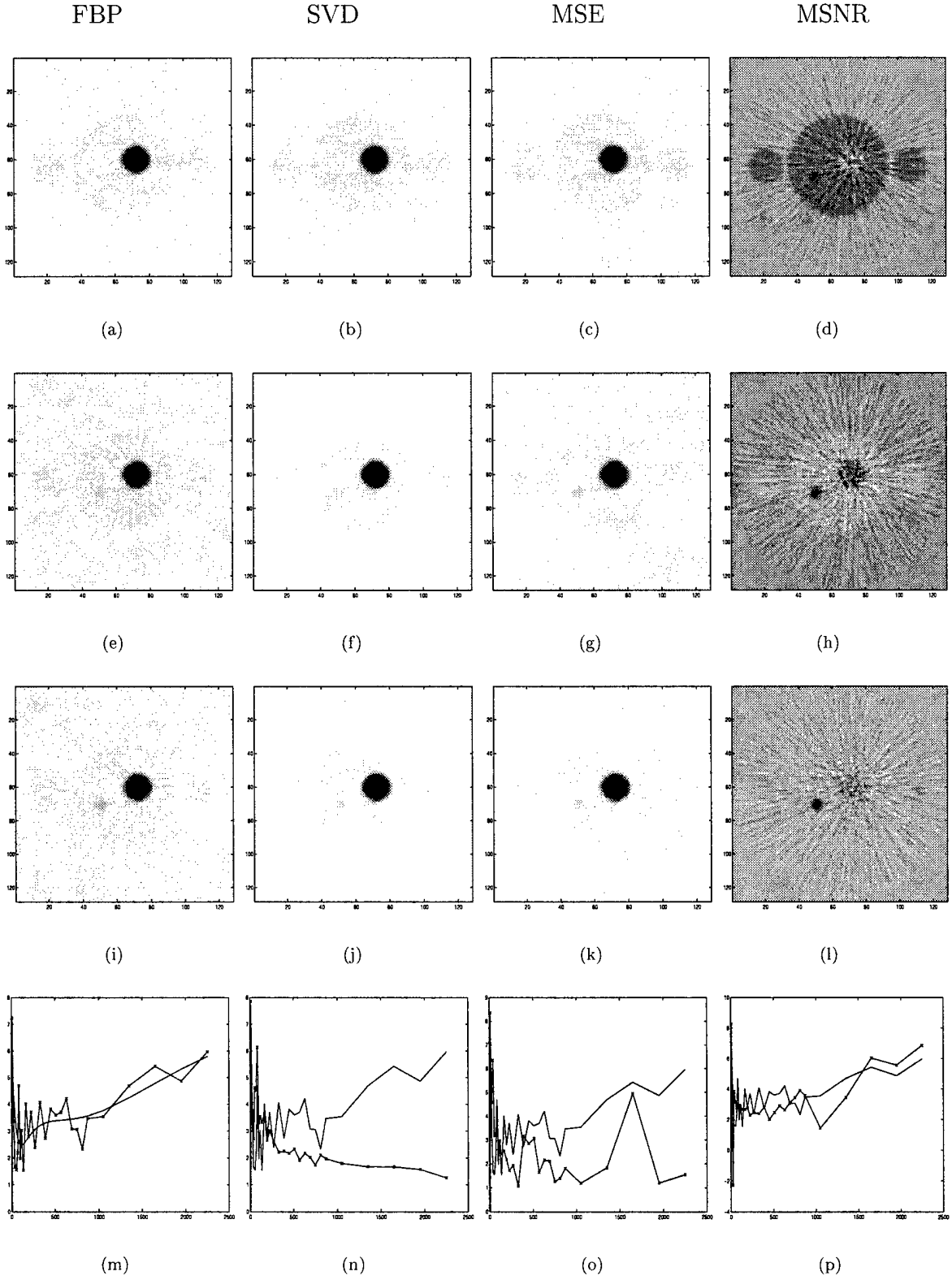

Figure 2: Reconstructed images: (a), (b), (c) and (d): the reconstructions of the 1^{st} frame, where "FBP", "SVD", "MSE" and "SNR" represent the reconstructions from the original sinogram, and the sinograms processed by the SVD, MSE, and maximum SNR methods; (e), (f), (g) and (h): the reconstructions of the 16^{th} frame; (i), (j), (k) and (l): the reconstructions of the 28^{th} frame; (m): the TACs of the lesion (the smallest circular region) in the phantom (solid line) and in the images reconstructed with no data compression (line with crosses); (n): the TACs of the lesion in the images reconstructed with no data compression (solid line) and with the SVD compression (line with crosses); (o): the TACs of the lesion in the images reconstructed with no data compression (solid line) and with the MSE compression (line with crosses) (p): the TACs of the lesion in the images reconstructed with no data compression (solid line) and with the maximum SNR compression (line with crosses);

Appendix D: Presentation at SNM Annual Conference 2000

Comparison of Kinetic Features in OSEM and FBP Dynamic PET Images for Oncology

X. Yu, C.C. Huang and P. S. Conti

PET Imaging Science Center, USC

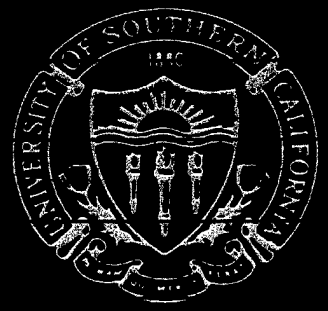

OBJECTIVE

- To study the advantages of OSEM over FBP in revealing
  - kinetic differences between normal tissues and lesions
  - kinetic similarity between primary tumors metastatses

IMAGES RECONSTRUCTION

- OSEM (ordered subset EM)
  - IEEE Trans. Nucl. Med. Dec. 1994
  - an approximation of EM algorithm
  - same order of computational complexity as FBP
- FBP (filtered backprojection)
  - built in CTI software on ECAT-953

4-K FDG COMPARTMENT MODEL

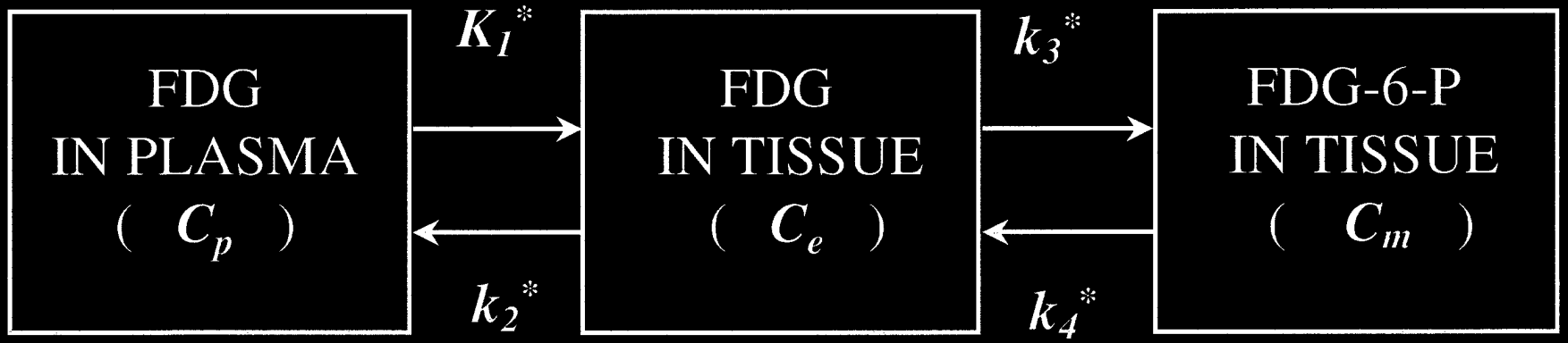

TAC: HOMOGENEOUS TISSUE

$$C^*(t)=C_e^*(t)+C_m^*(t)=(a_1e^{-\beta_1 t}+a_2e^{-\beta_2 t})\otimes C_p^*(t)$$

$$C_{total}^*(t)=v_pC_p^*(t)+(a_1e^{-\beta_1 t}+a_2e^{-\beta_2 t})\otimes C_p^*(t)$$

TAC: HETEROGENEOUS TISSUE

$$\overline{C}^{*}(t) = \sum_{j=1}^{J} w_j \left(a_{1,j} e^{-\beta_{1,j} t} + a_{2,j} e^{-\beta_{2,j} t} \right) \otimes C_p^{*}(t)$$

$$= \sum_{k=1}^{I} \alpha_k e^{-\beta_k t} \otimes C_p^{*}(t)$$

$w_{j,\cdot}$ ***mixture coefficient***

α_k: **weighting coefficient**

$e^{-\beta k\, t}$: **physiological factor**

HYPOTHESES

- The physiological functions (factors) in primary tumors and metastatses shall be similar in a given organ
- The physiological features of visible lesions can be applied to identify invisible lesions

RATIONALE

- TAC of lesions in PET-FDG dynamic images increases with time

- Normal tissue TAC decreases in most organs

METHOD

- Kinetic features are compared in three forms
  - –TACs in ROI
  - – compartment parameters
  - – physiological factors

CRITERIA FOR COMPARISON

- Mean squares error for TAC
- Distance between two parameter clusters for compartment parameters
- Receiver operating characteristic for physiological factors

Hypothesis Test Statistic: Likelihood Ratio

- Suppose the physiological factors are obtained for a known tumor and known normal tissues
- For an given ROI, the hypothesis test computes the likelihood that the observed TACs are
  - in a lesion or
  - in normal tissues

IMAGE CORRECTIONS

- Image corrections include:
  - attenuation correction
  - decay correction
  - dead time correction

DATA for STUDAY

- Experimental phantom:
  - uniform cylinder
- Computer generated phantom:
  - containing 250 artificial lesions
- Clinic study:
  - 8 proven lung cancers
  - 8 proven breast cancers

Results: Lung Cancer (fbp)

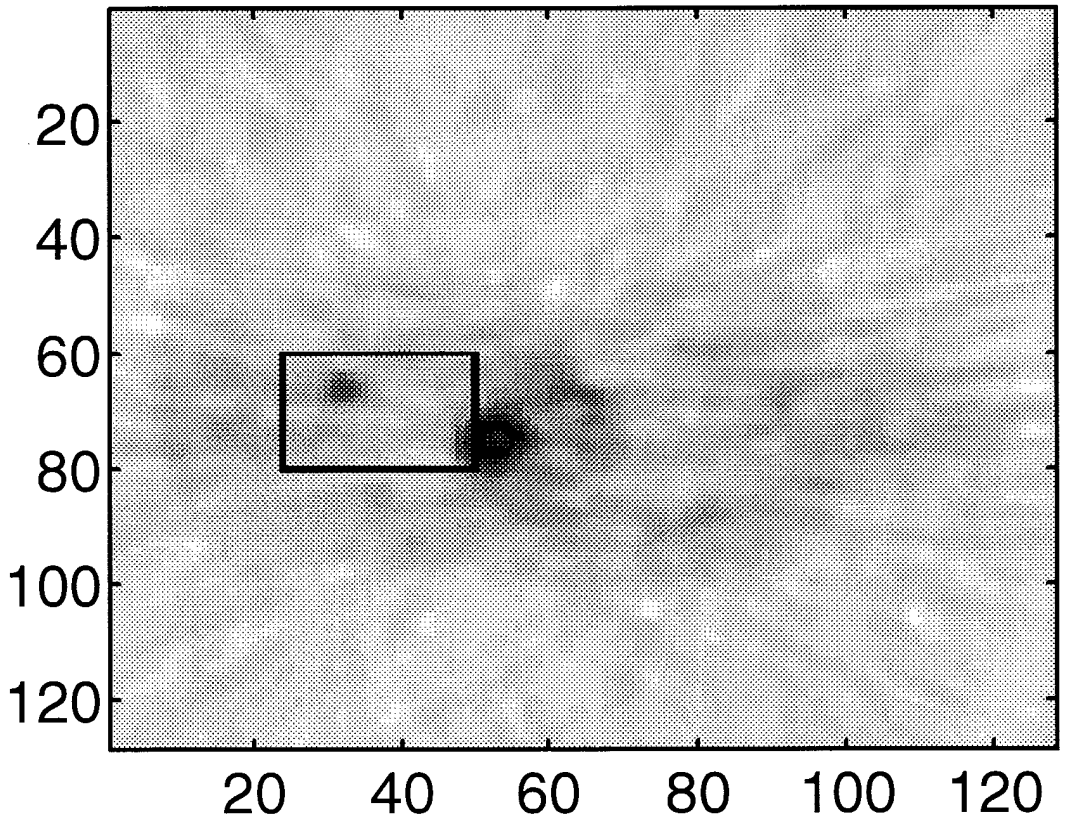

Results: Lung Cancer (OSEM)

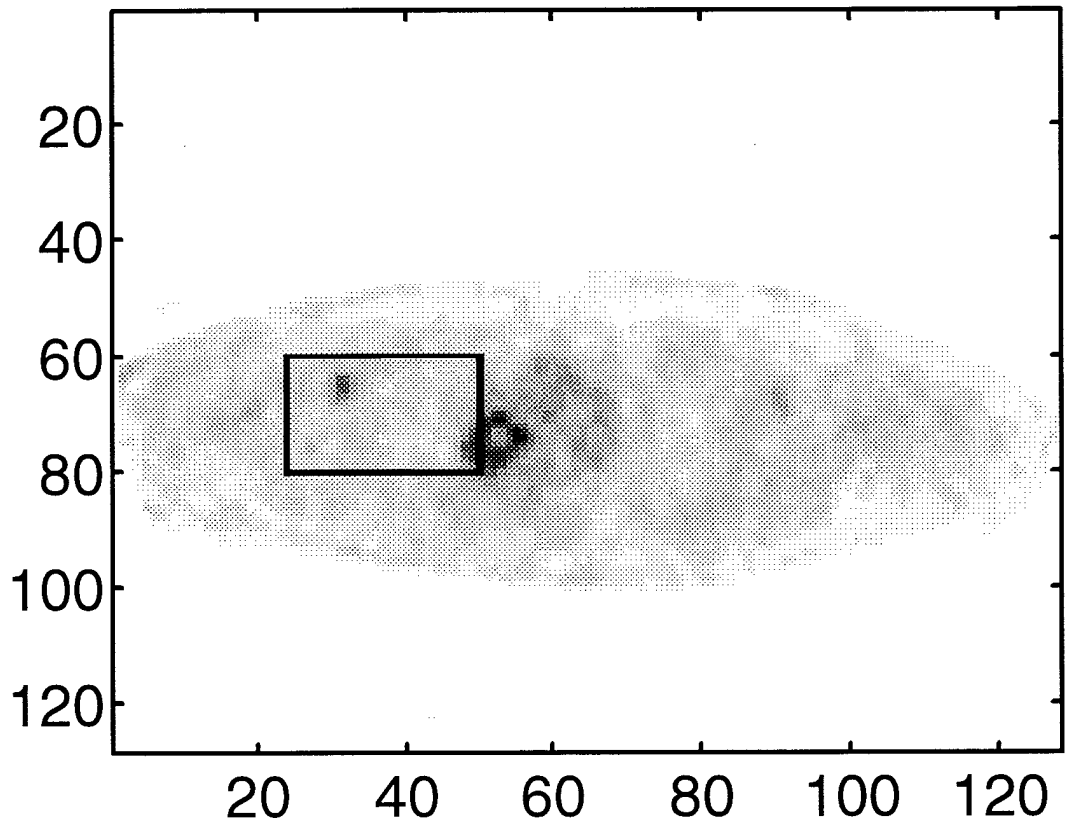

Lung Cancer: TAC

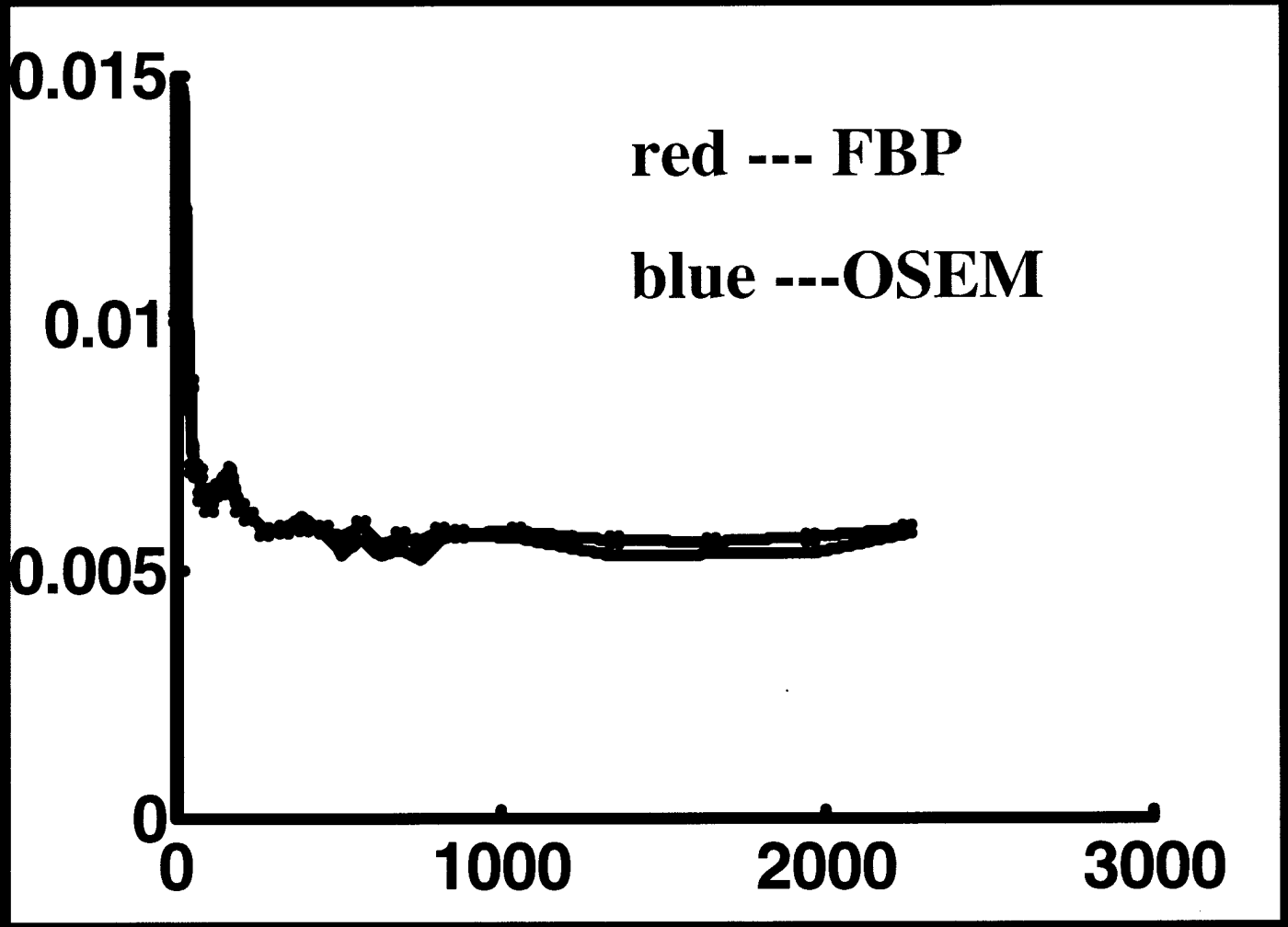

Likelihood Values: Lung Cancer

FBP

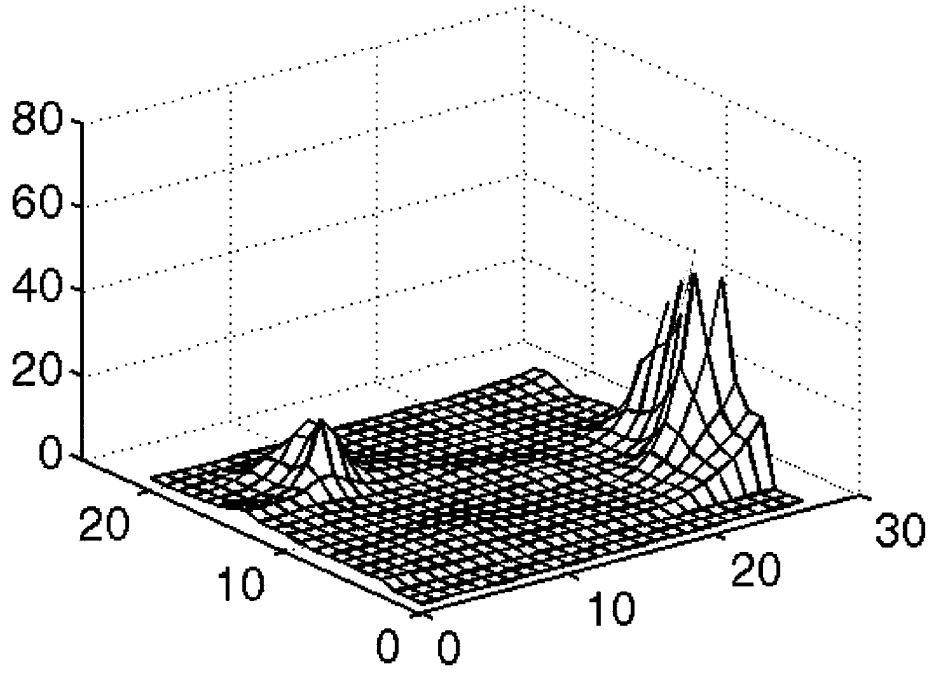

OSEM

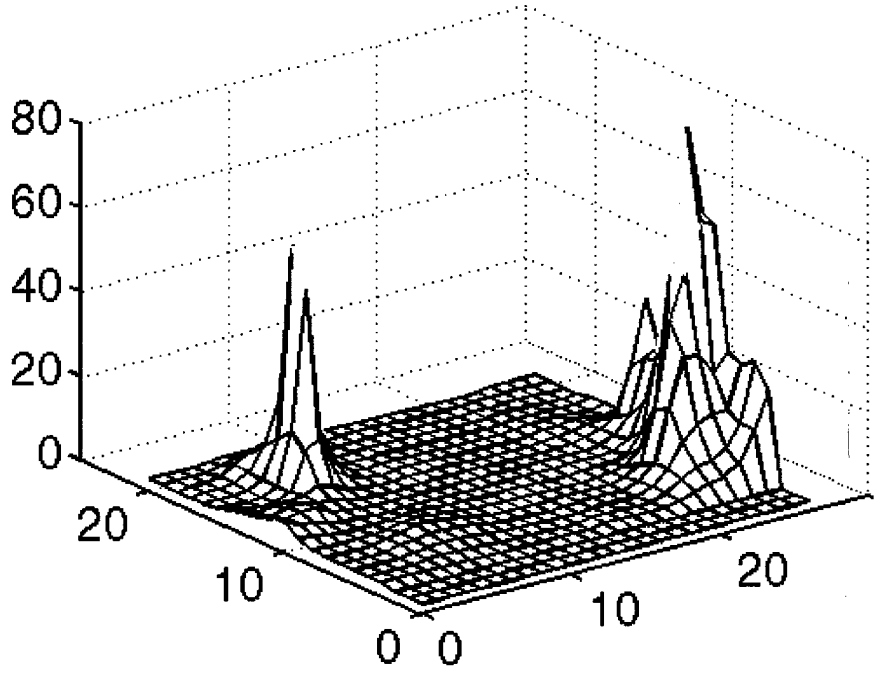

Likelihood Values: Lung Cancer

FBP

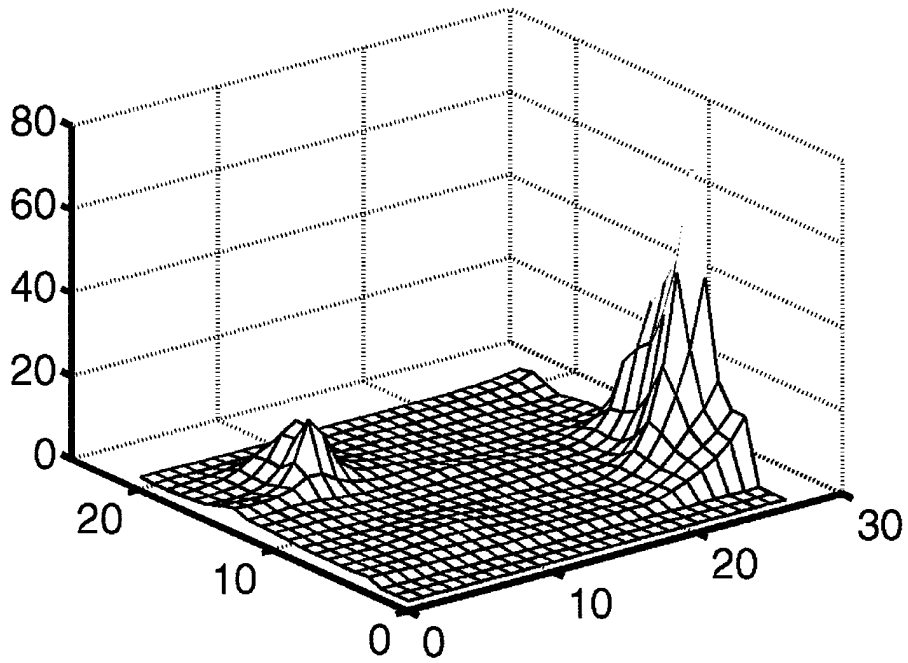

OSEM

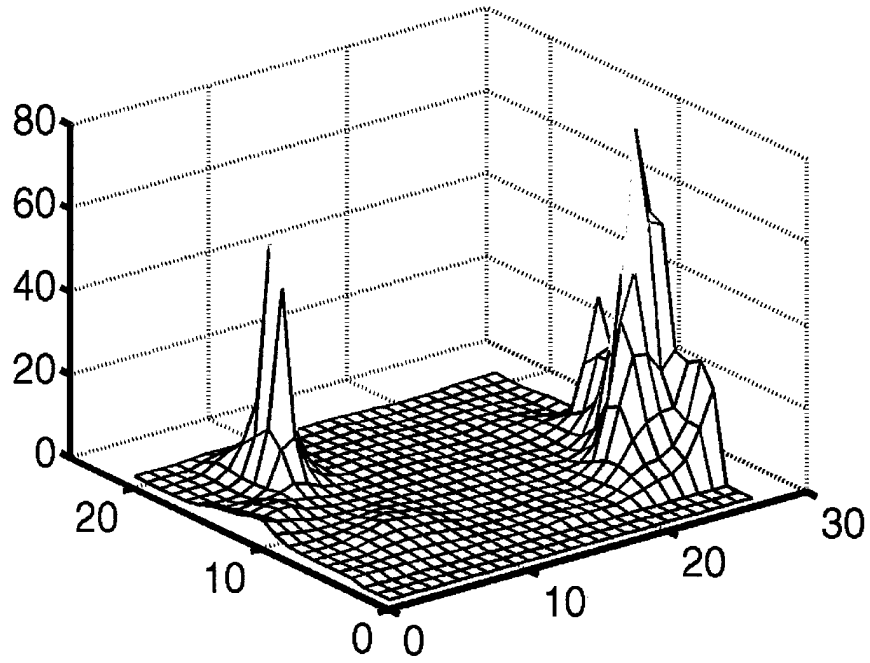

Results: Breast Cancer (fbp)

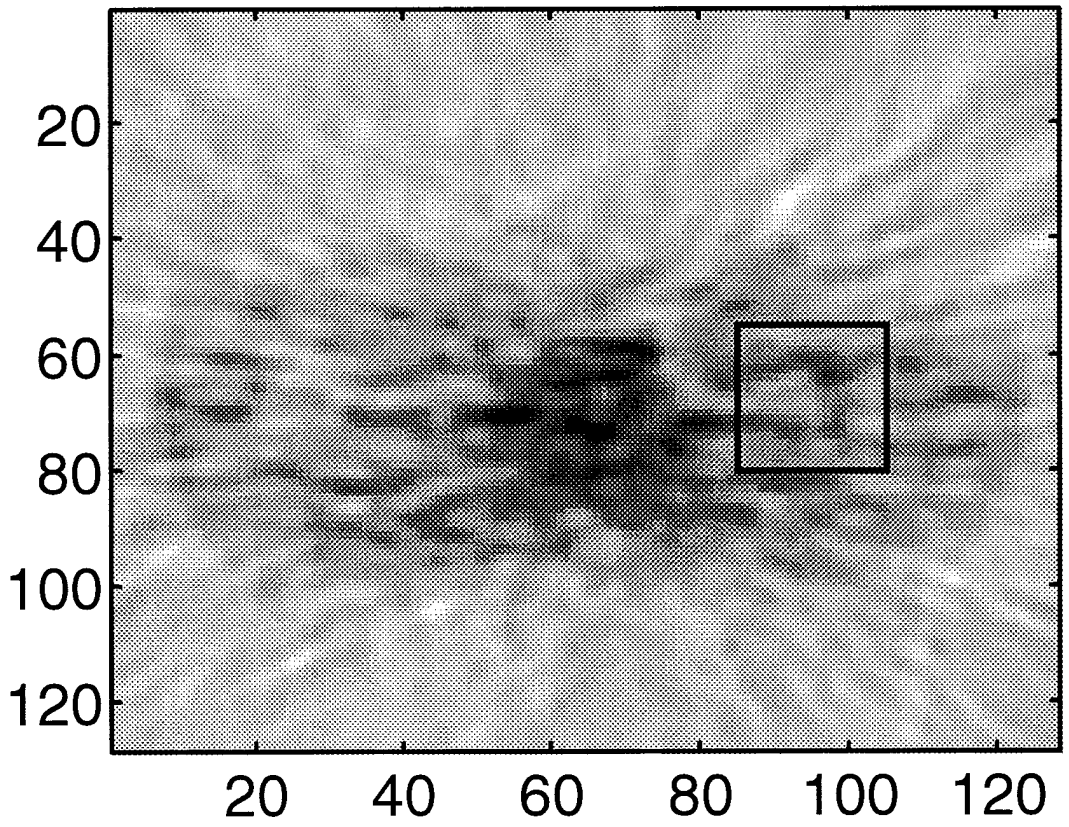

Results: Breast Cancer (OSEM)

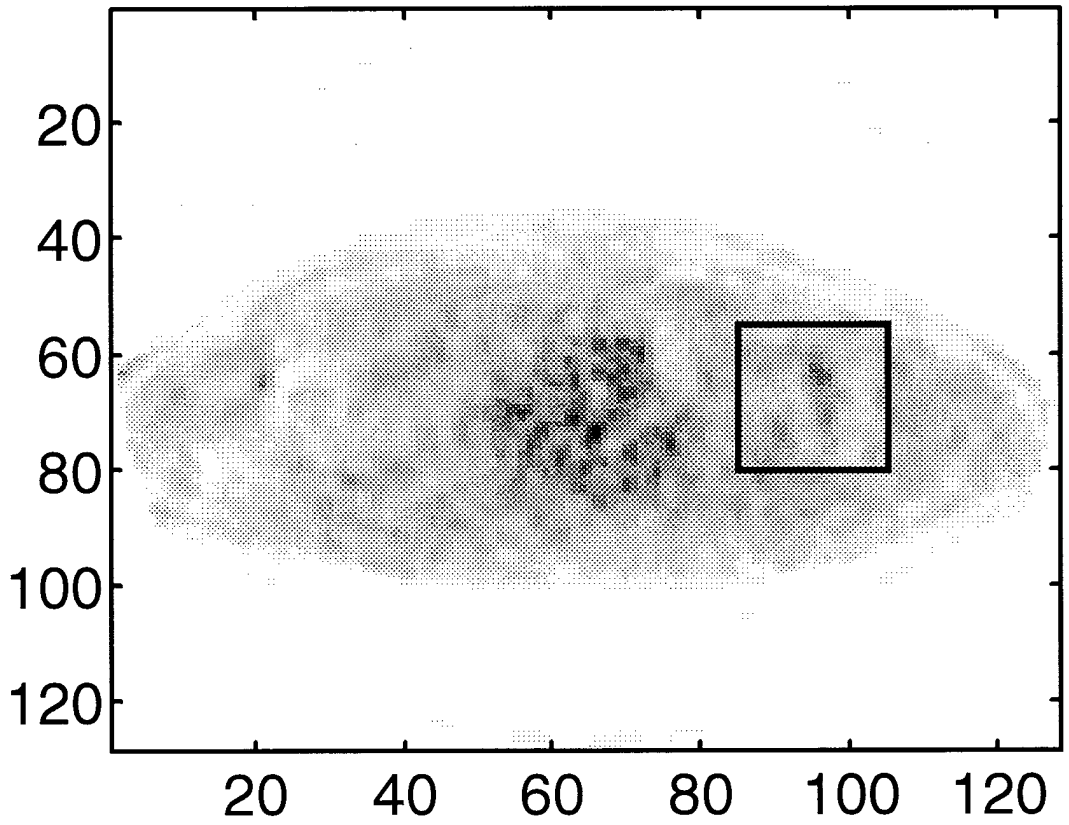

Breast Cancer: TAC

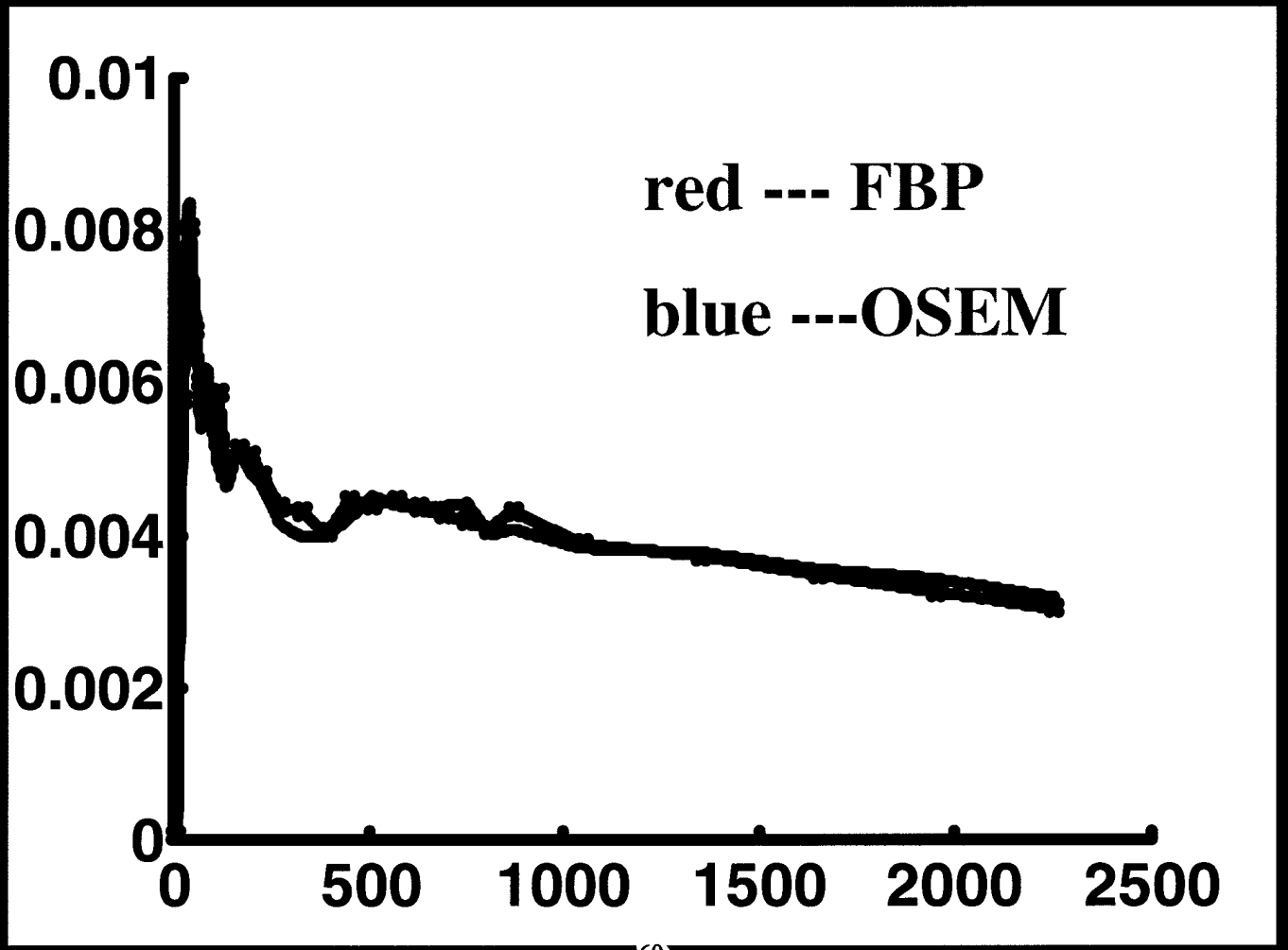

Likelihood Values: Breast Cancer

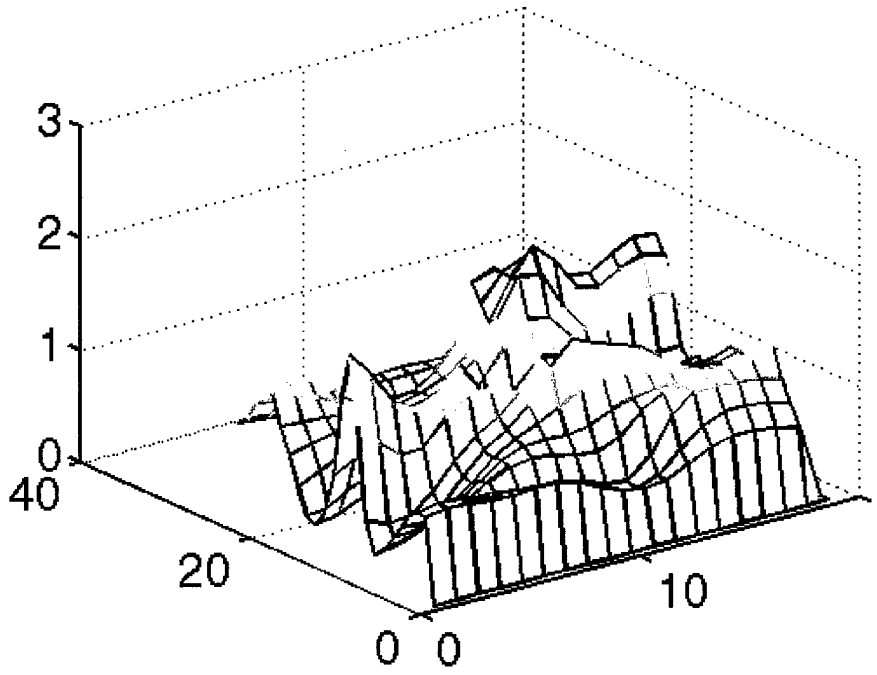

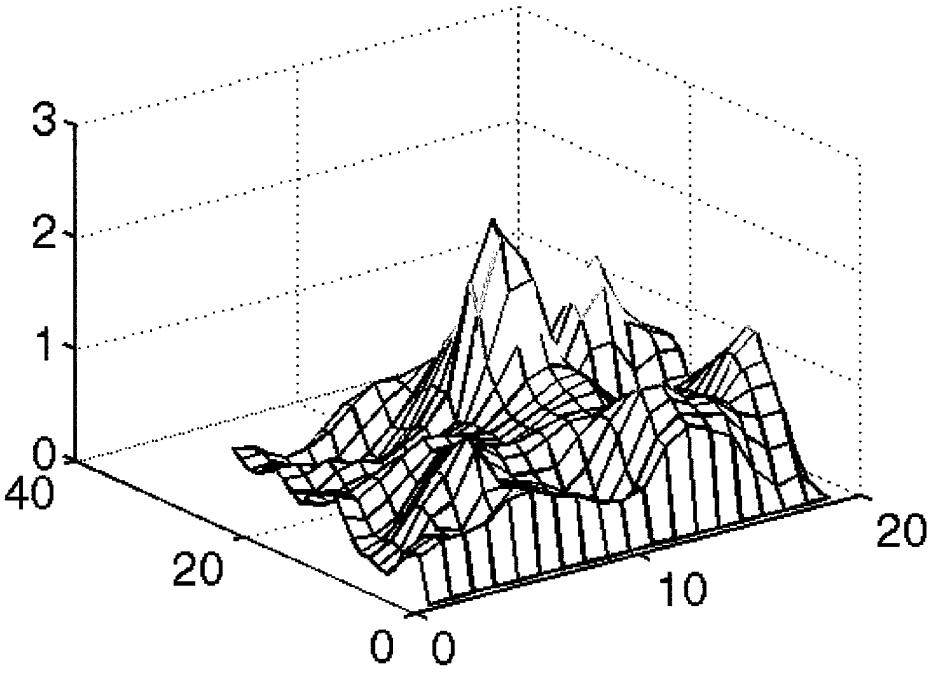

Likelihood Values: Breast Cancer

FBP

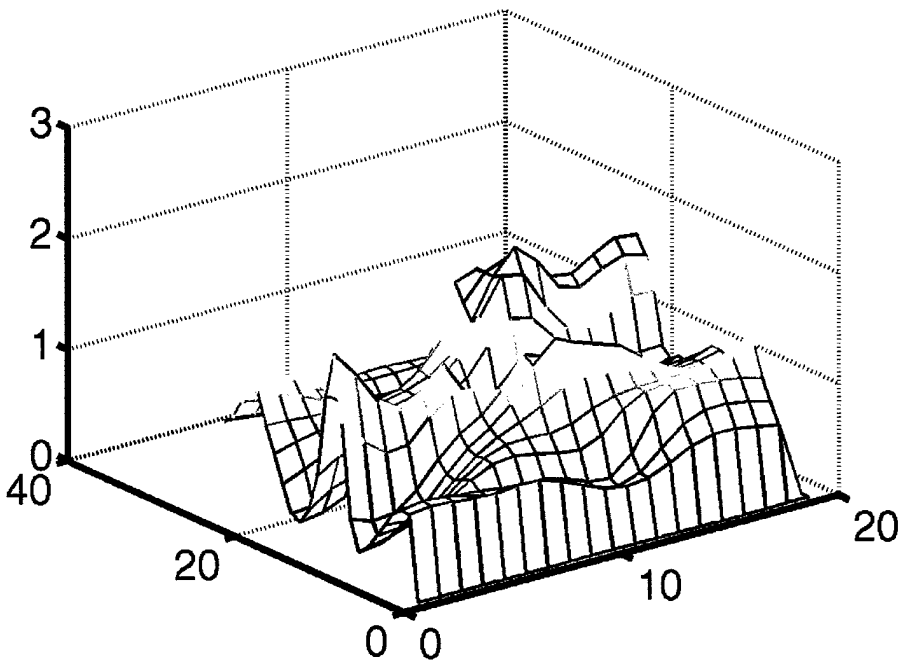

OSEM

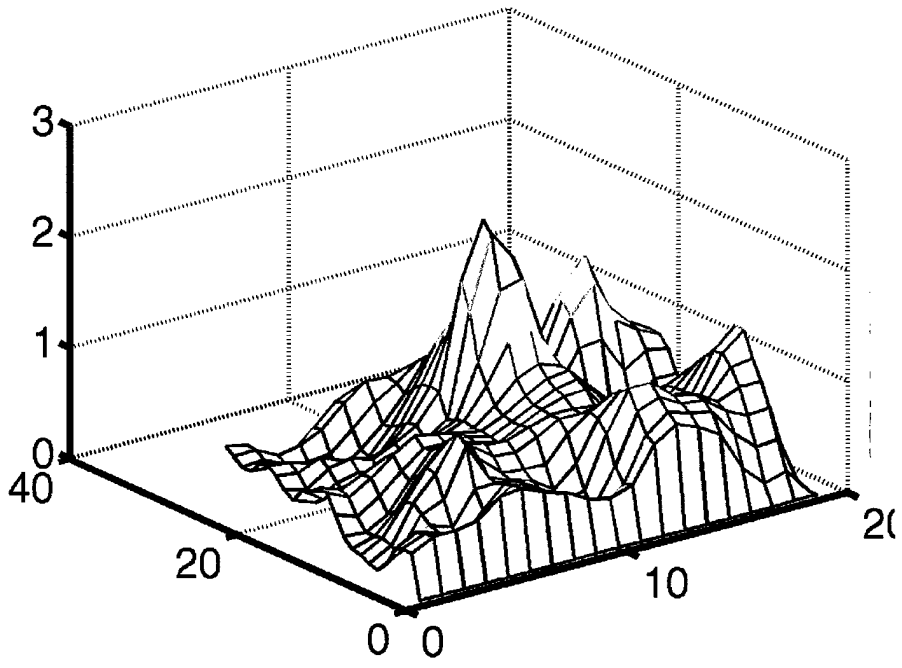

Quantification: Lesions

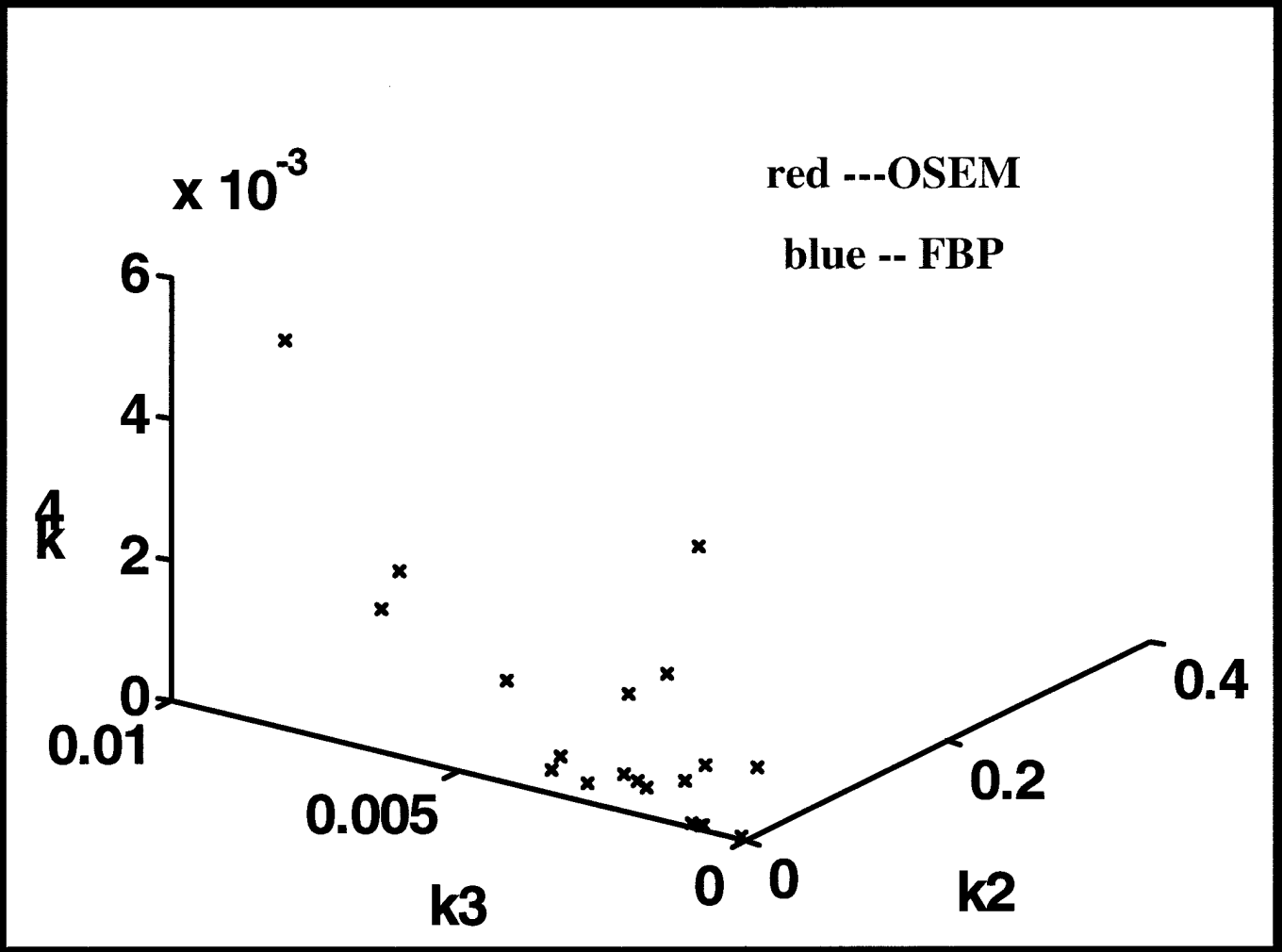

Lesion Clusters

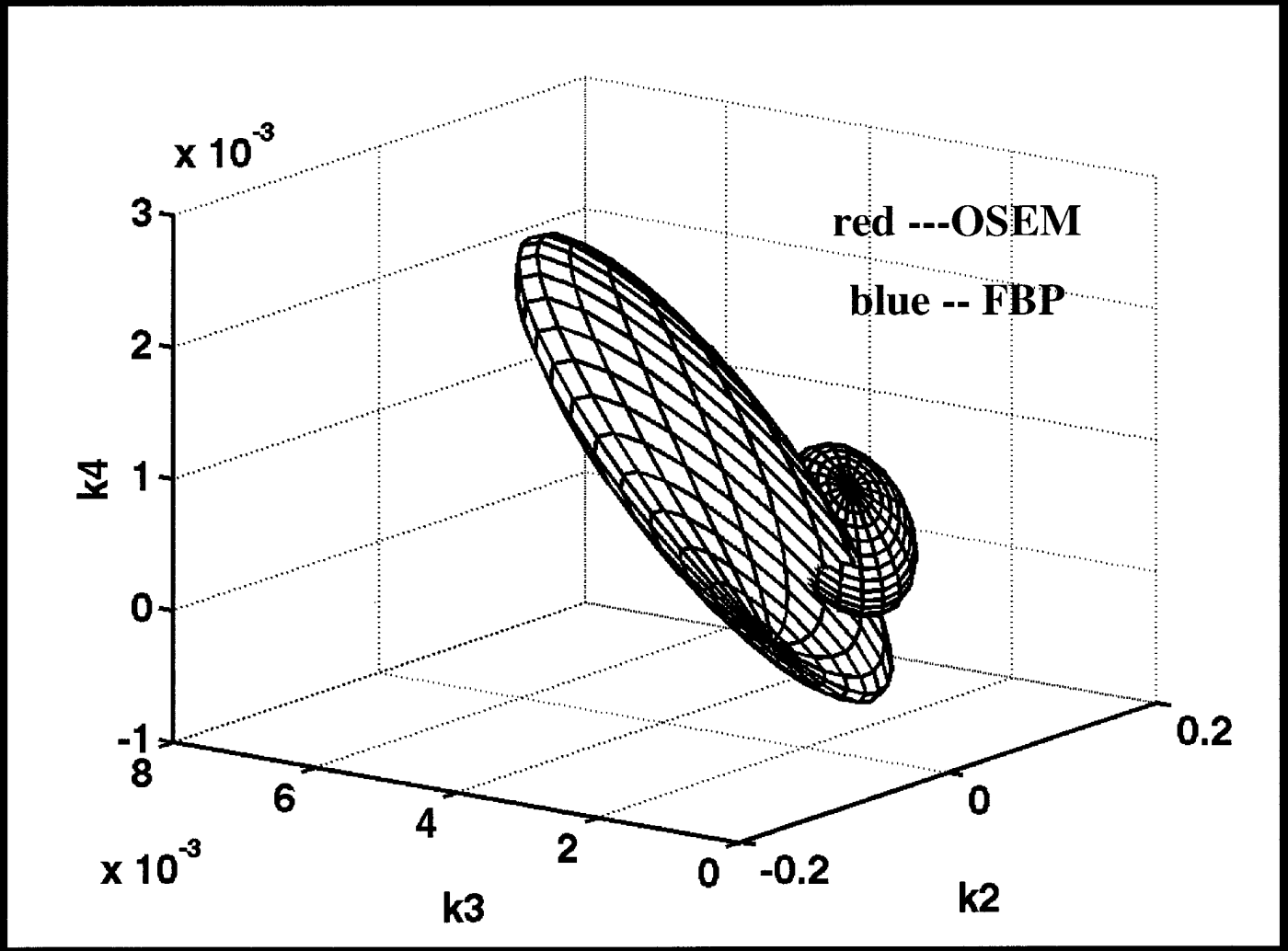

Quantification: Lesions and Normal Tissues

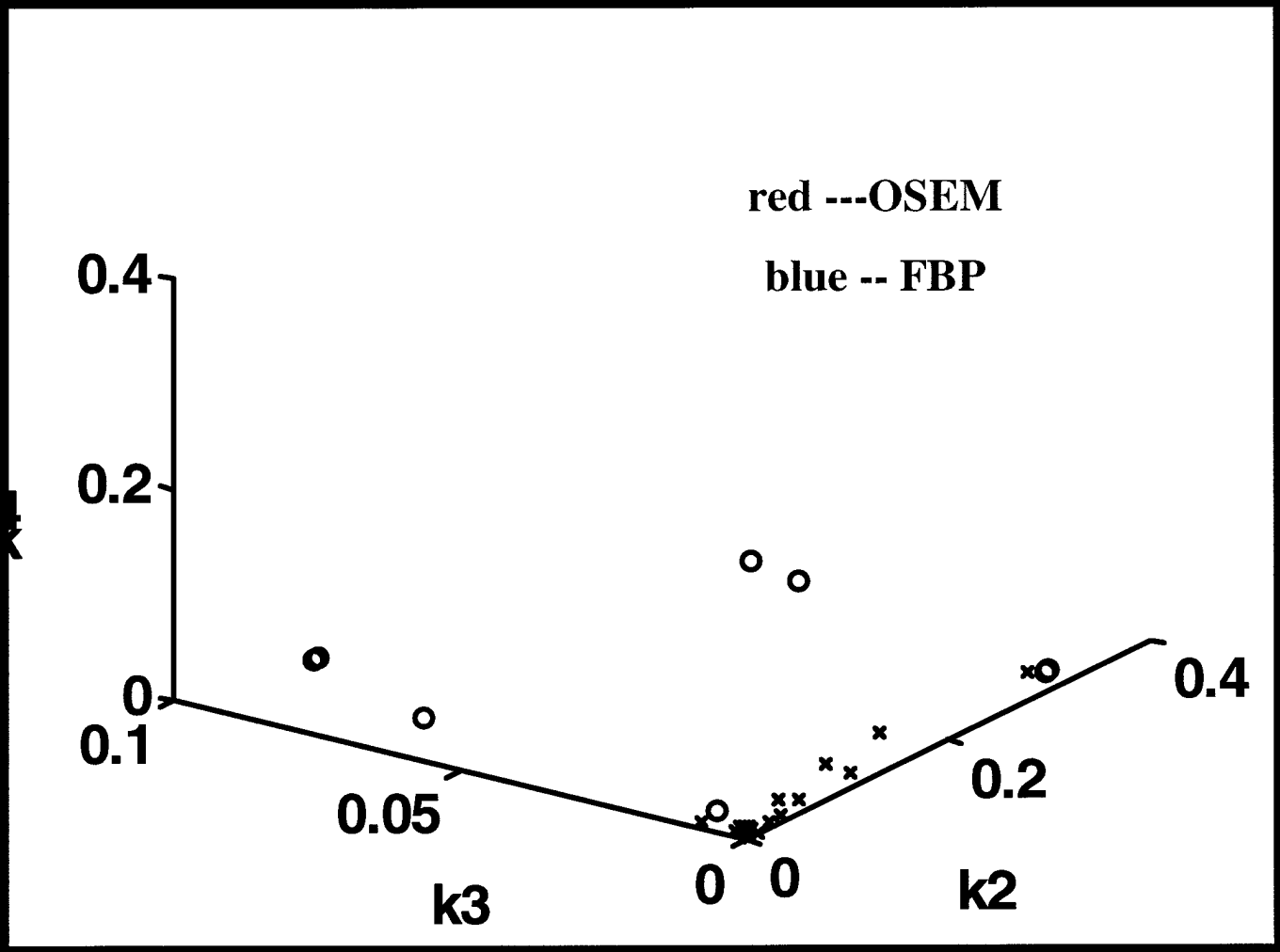

Phantom

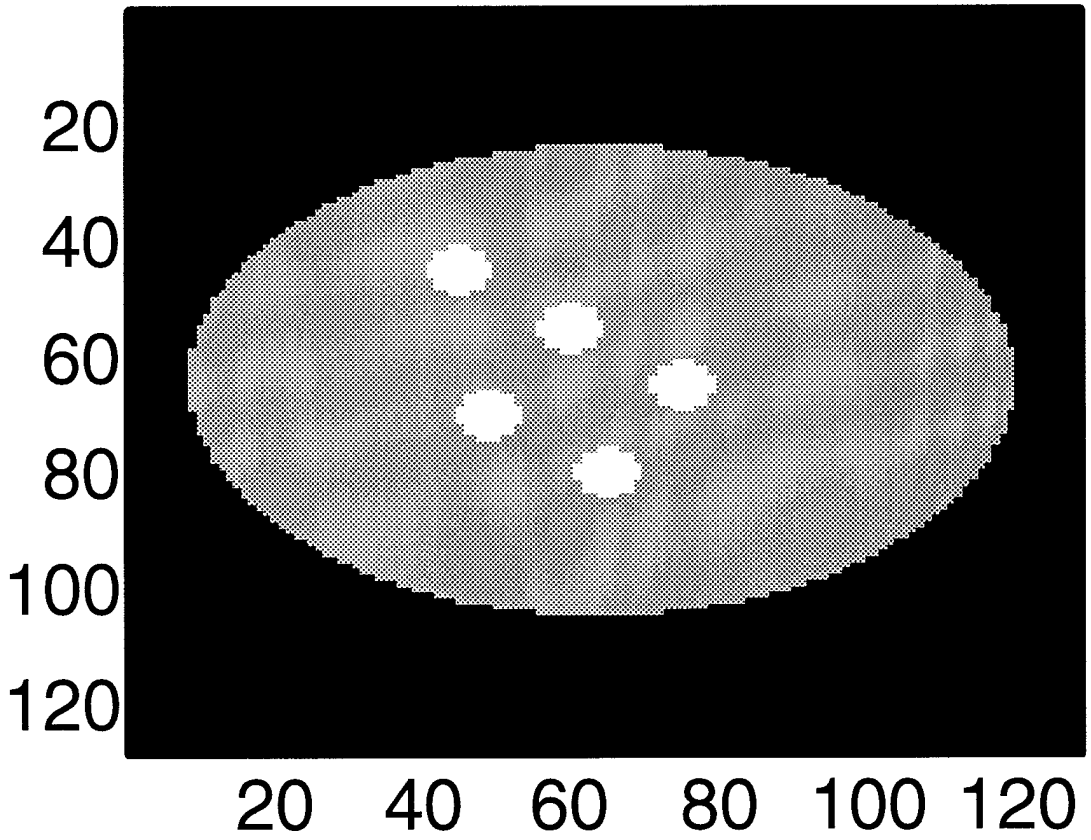

Phantom: FBP

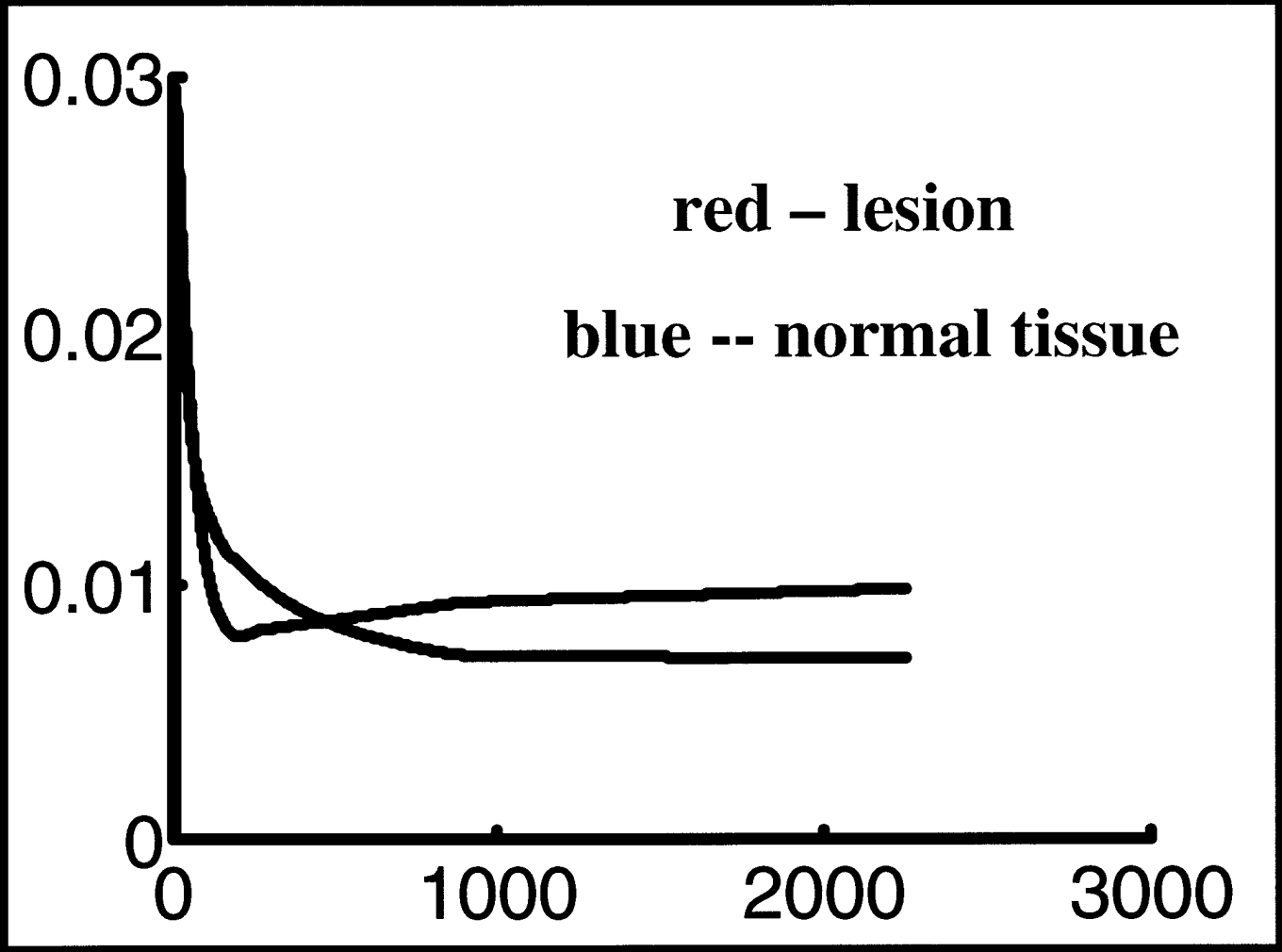

Phantom: FBP

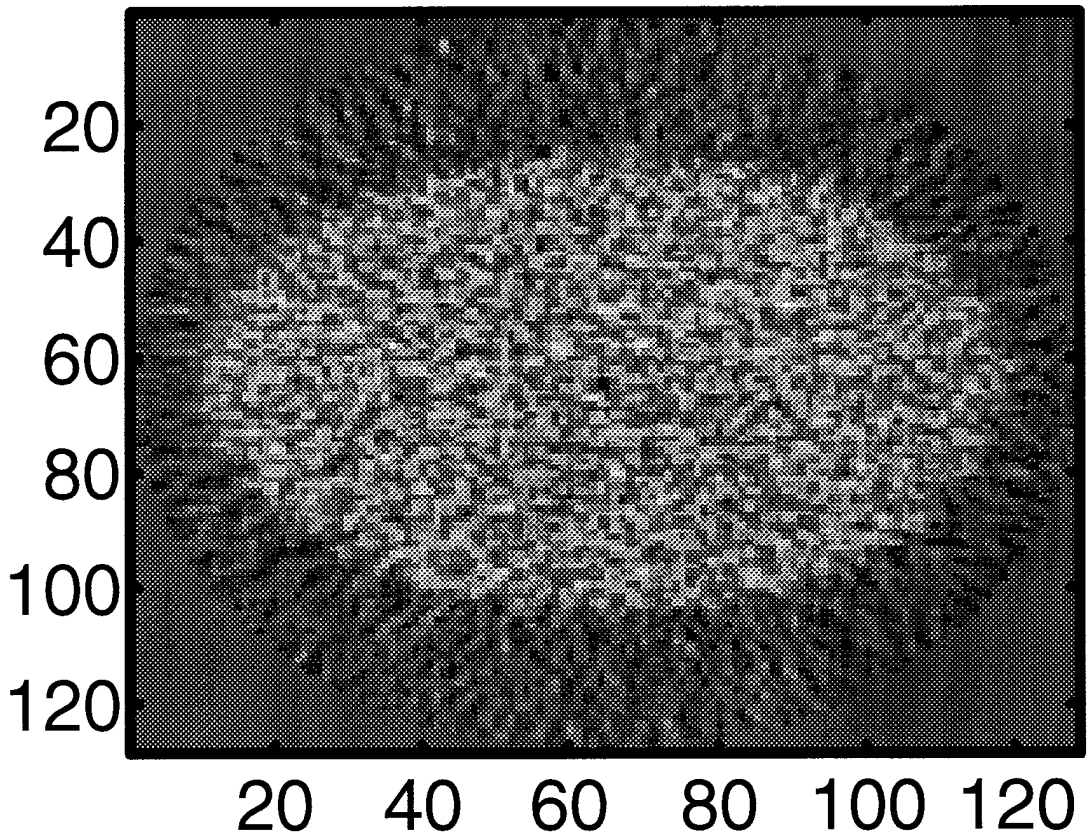

Phantom: OSEM

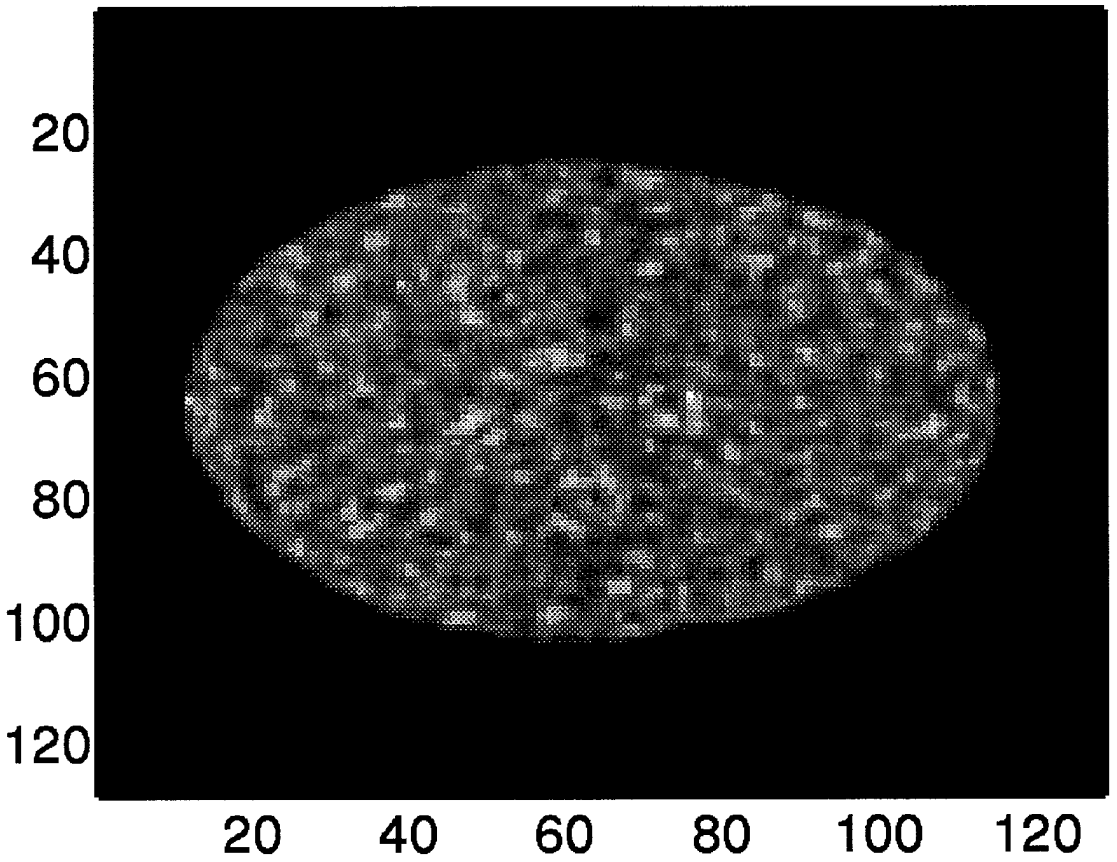

ROC Comparison

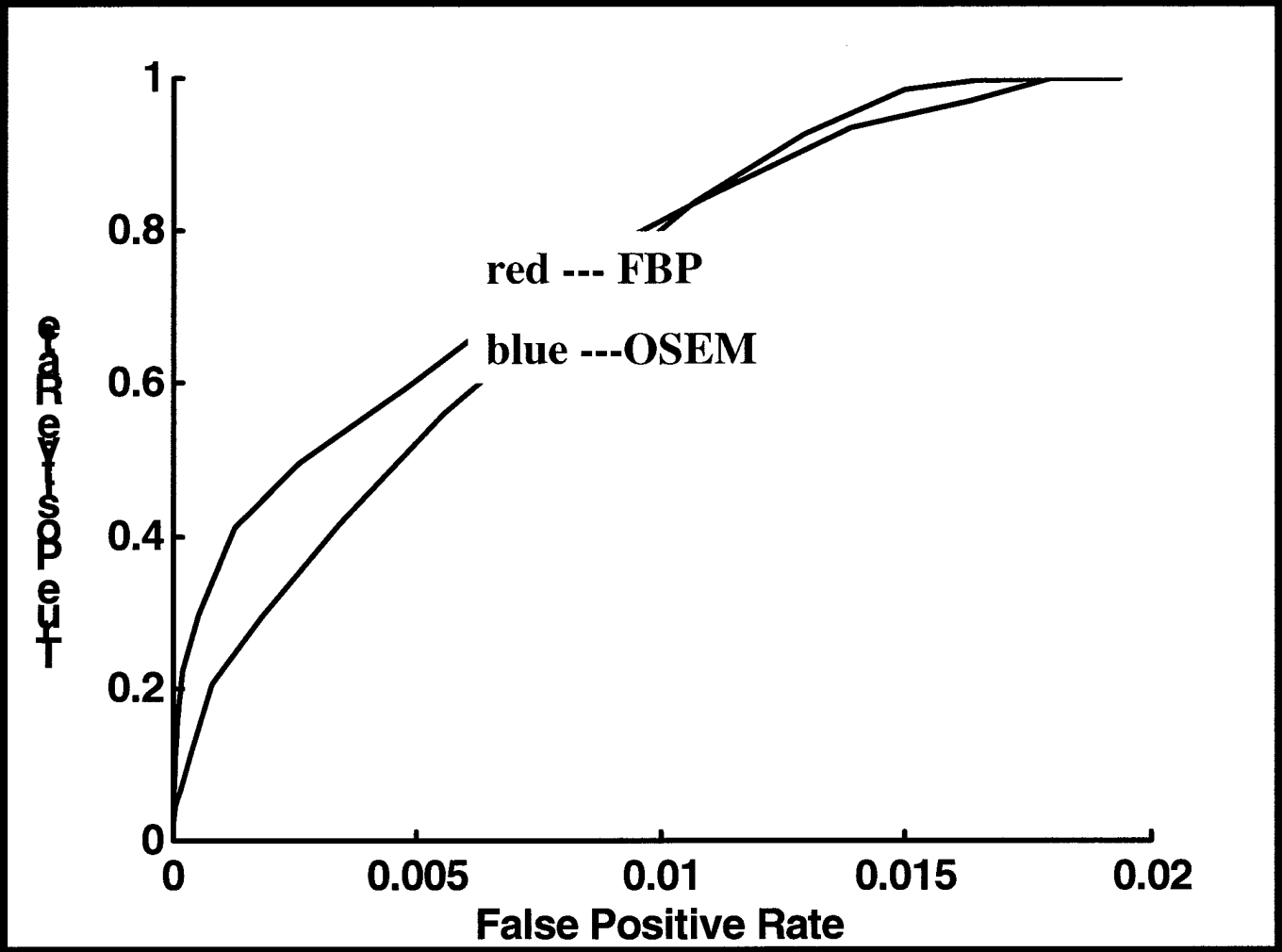

CONCLUSION

- No significant difference observed in TACs for OSEM and FBP images
- The physiological similarity between primary tumor and metastatses can be revealed more clearly in OSEM images.
- OSEM is potential for improving the sensitivity of metastasis detection.